



Statistical Significance of Mission Parameters on the Deflection Efficiency of Kinetic Impacts: Applications for the Next-generation Kinetic Impactor

Mallory E. DeCoster¹, Emma S.G. Rainey, Thomas W. Rosch, and Angela M. Stickle¹

The Johns Hopkins University Applied Physics Laboratory, 11100 Johns Hopkins Road, Laurel, MD 20723, USA; mallory.decoaster@jhuapl.edu

Received 2021 November 30; revised 2022 June 6; accepted 2022 June 21; published 2022 August 8

Abstract

Understanding how to deflect an incoming asteroid is of great importance and a focus of research undertaken internationally by the planetary defense community. Deflection of an asteroid by a kinetic impactor is one such mitigation method that has a high degree of technological maturity. In 2022, NASA’s planetary defense mission, the Double Asteroid Redirection Test (DART), will provide the first full-scale technology demonstration of a kinetic impactor. However, the DART mission is just a single test of one kinetic impactor design, prompting the question: Is it possible to optimize the design of a kinetic impactor to make it the most efficient deflector that it can be? In this paper, we use high-fidelity hydrodynamic simulations to examine the effect of five mission parameters (impactor mass, impact velocity, impactor composition, impactor geometry, and target strength) on three observables related to deflection efficiency (crater morphology, ejecta distribution, and momentum transfer) resulting from kinetic impacts. We find that the most significant mission parameters for determining postimpact factors are the impact velocity, impactor mass, and target strength. The impactor geometry and impactor composition emerge as statistically nonsignificant. Overall, we find that the ogive impactor geometry results in the highest variance in predicting the momentum enhancement factor (β), and that generally, impactors with smaller volumes and flat leading edges (plates and rings) produce smaller craters and less ejecta mass compared to impactors with larger volumes and sharper leading edges (spheres, ogives, and cones).

Unified Astronomy Thesaurus concepts: [Impact phenomena \(779\)](#); [Planetary science \(1255\)](#)

1. Introduction

Asteroid impacts pose a credible threat to Earth. While impacts that cause global-scale devastation (such as the Chicxulub asteroid impact that preceded the end-Cretaceous mass extinction affecting the dinosaurs; Alvarez et al. 1980; Schulte et al. 2010; Bardeen et al. 2017) are unlikely; more recent examples, like the Tunguska (Robertson & Mathias 2019) and Chelyabinsk (Popova et al. 2013) events, attest that even asteroids tens of meters in size are a cause for concern. These contemporary examples have drawn attention to the reality that impacts of this type are a serious natural hazard and have spurred interest in research in planetary defense, because asteroid impacts are a potentially preventable natural hazard.

The kinetic impact method is a promising strategy for asteroid deflection that exhibits a high degree of technological maturity (National Research Council 2010; Dearborn & Miller 2015). A kinetic impactor concept for asteroid deflection relies on smashing a large spacecraft (“impactor”) into the potentially hazardous object (PHO; “target”) at a high impact velocity ($\sim 2\text{--}15\text{ km s}^{-1}$) in order to impart a change in the velocity (and momentum). A change in the target’s velocity then results in a small change in the orbit of the target, such that the asteroid no longer collides with Earth.

Generally, two main variables control the initial kinetic impact effect (i.e., velocity change of the orbit of the PHO): the relative velocity vector of the impact and β , which is a measure of the total momentum enhancement imparted to the asteroid. The momentum enhancement factor, β , relates the

instantaneous change in velocity (Δv) experienced by a PHO from a kinetic impact to the mass of the target and the input momentum from the impactor (Cheng et al. 2016; Stickle et al. 2020). In a kinetic impact, β contains components from the impactor momentum, as well as contributions from the ejecta produced by the impact crater. The resultant ejecta may produce additional thrust so that β is greater than 1. Therefore, an efficient kinetic impactor should seek to optimize Δv and β by maximizing the resultant excavated ejecta momentum from the impact.

The extent to which β can be optimized remains an open question because it depends on asteroid parameters that can have rather high uncertainties, such as the local topography at the impact site and target material properties like cohesion and porosity (Stickle et al. 2015; Cheng et al. 2016; Raducan et al. 2019). Previous experimental and computational work has shown that β depends on the impact velocity (Holsapple & Housen 2012), target material properties (i.e., strength, porosity, cohesion, and internal friction; Tedeschi et al. 1995; Holsapple & Housen 2012; Walker et al. 2013; Bruck Syal et al. 2016; Raducan et al. 2019; Rainey et al. 2020; Walker et al. 2020), and impactor properties (Ikeda et al. 2017). While it is impossible to control the composition or morphology of a real asteroid (though such properties could be constrained by a reconnaissance mission, if time allowed), there is opportunity to tailor the design of the impactor. The effects of impactor composition and morphology (i.e., mass placement within the impactor) on β are poorly understood and could emerge as a useful design parameter as the kinetic impactor technology matures. To this end, it may be possible to optimize the next-generation kinetic impactor for planetary defense by tuning the mass placement using different impactor geometries.



Original content from this work may be used under the terms of the [Creative Commons Attribution 4.0 licence](#). Any further distribution of this work must maintain attribution to the author(s) and the title of the work, journal citation and DOI.

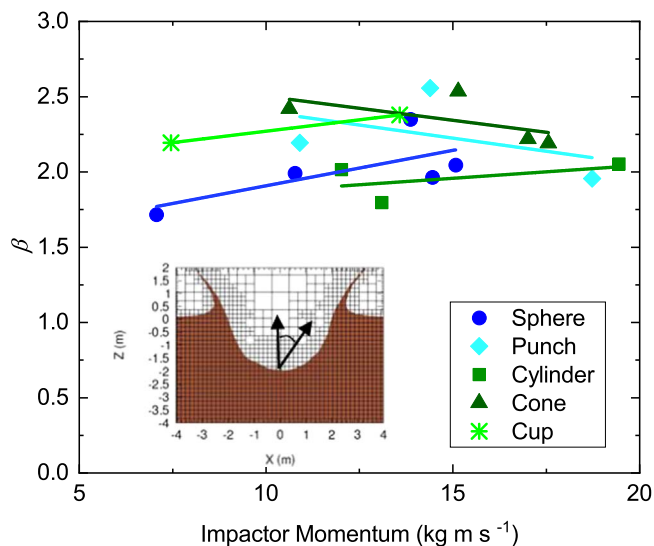


Figure 1. Experimental results replotted from Ikeda et al. (2017). Lines represent a linear fit to the data points to show approximate trends. In total, Ikeda et al. showed that the impactor geometry does not affect the ejecta mass but does affect β because impactors that promote large ejecta emission angles (α) result in a smaller β . The inset shows the crater formed in an exemplar CTH simulation and corresponding α .

Studies on munitions ballistics and previous experiments with ballistic pendulums paired with light gas guns offer some insight into the role of impactor geometry on cratering and momentum enhancement. It is well known in munitions ballistics that the ballistic properties of penetrating impactors (i.e., mass, nose contour, and the addition of jackets that protect against friction from the barrel and help control deformation at impact) lead to different effects determined by the interaction between the impactor and target (Harvey 1948; Backman & Goldsmith 1978; Stefanopoulos et al. 2014). In munitions ballistics, increased damage is often achieved through the deformation of expanding bullets upon impact, which substantially enhances the energy transfer to the target and increases the crater’s diameter. Although the impactor momentum of a bullet is approximately 5 orders of magnitude smaller than what would occur at planetary defense scales, lessons learned from munitions ballistics motivate the consideration of impactor parameters toward designing kinetic impactors for planetary defense. Namely, it may be possible to optimize the rate of momentum transfer to the target material by tuning the shape (i.e., frontal surface area) of the impactor.

Previous studies on the effect of impactor shape on momentum enhancement are quite sparse. Ikeda et al. (2017) presented results from a two-stage light gun that launched five different aluminum impactor geometries into a firebrick target (density = 2.0 g cm^{-3}) mounted on a ballistic pendulum to measure β . Figure 1 replots a subset of their findings in addition to lines representing a linear fit ($ax + b$) to the data, which captures the general trends. Figure 1 shows that there is not one impactor geometry that outcompetes the others for achieving the largest β ; however, an impactor geometry effect is evident. The lines show that β increases with input momentum for the sphere, cylinder, and cup impactors; however, β decreases with impactor momentum for the punch and cone impactor over the incident impactor momentum ranges sampled. The discrepancy between trends warrants further investigation into the effects of impactor geometry on β .

Ikeda et al. showed that while the impactor shape does not affect the excavated ejecta mass, different impactor shapes do influence β by controlling the angle of ejection. They concluded that the influence of ejecta mass on β for each shape is different because of the ejecta spread angle (α), where a large α results in a smaller β . Therefore, considering a vertical impact with the standard definition of the normal-component enhancement factor (Cheng et al. 2016; Rivkin et al. 2021), these results suggest that impactors that promote an ejecta curtain resembling a concentrated beam in the direction normal to the surface target will outperform those that result in ejection that is more diffuse. In total, previous studies suggest that not all impactor mass is treated equally when contributing to the momentum enhancement mechanisms at play in a kinetic impact. Therefore, they provide sound evidence that motivates further investigation into the optimization of impactor design concepts toward more efficient kinetic impactor deflections.

In addition to the small-scale experimental results previously discussed, there are a few examples of large-scale impactor missions that include penetrator-type spacecraft concepts like Deep Impact (A’Hearn et al. 2005) and the Lunar Crater Observation and Sensing Satellite (LCROSS; Schultz et al. 2010), as well as the ongoing Double Asteroid Redirection Test (DART) mission (Cheng et al. 2018). These missions provide some experimental evidence for the role of impactor shape on the crater and ejecta distribution resulting from hypervelocity impact at spatial scales relevant to planetary defense. For example, the Deep Impact mission concept consisted of a 370 kg platelike impactor with a thick copper shield that was designed to penetrate the surface of a comet (Tempel-1) to generate an $\sim 100 \text{ m}$ wide by $\sim 25 \text{ m}$ deep crater (A’Hearn et al. 2005). A unique feature of the Deep Impact penetrator was the use of a copper plate ($\sim 100 \text{ kg}$) located on the encounter end of the impactor, intended to protect Deep Impact from the comet’s debris field before the encounter. The impact result produced an ejecta curtain of hot ($>1000 \text{ K}$) gas and dust and uncovered very low shear strength ($<65 \text{ Pa}$) material lying within tens of meters of the surface; it also produced a 200 m diameter excavation crater with a small mound in the center (A’Hearn et al. 2005; Schultz et al. 2013). Deep Impact is a useful test case for considering the usefulness of components like heavy copper shields applied to kinetic impactor missions. In addition, LCROSS repurposed the spent upper stage of the Atlas V rocket launch vehicle (Centaur rocket) as a kinetic impactor and monitored the evolution of the resulting ejecta from its collision with the lunar surface (Colaprete et al. 2010; Schultz et al. 2010). The impactor resembled an ogive shape (the roundly tapered end of a 3D cone, similar to the shape of a streamlined bullet) with a diameter of approximately 3 m and an empty mass of approximately 2200 kg (United Launch Alliance, LLC 2021). The collision produced a crater about 25–30 m across with about 400–6000 kg of ejecta exhibiting both low and high ejection angles, an evolution attributed to the nature of the impactor (Schultz et al. 2010). Lastly, the DART impactor is also an important end-member that consists of an approximately 535 kg cuboid bus containing large solar panel wings extended on either side. The DART spacecraft will deliberately impact itself into the moonlet (Dimorphos) of the binary near-Earth asteroid (65803) Didymos to change its orbital period. The DART impact will occur in late 2022 September, and measurements of the crater size and ejecta distribution will occur to aide in the determination of the efficiency of a kinetic impactor toward deflection mitigation.

Altogether, the Deep Impact, LCROSS, and DART impactors display a realistic variety in impactor geometry that could be achieved in the design of a viable kinetic impactor spacecraft.

This work computationally investigates the effects of five mission parameters (impactor mass, impact velocity, impactor geometry, impactor composition, and target strength) on the crater morphology, ejecta distribution (mass and velocity), and momentum enhancement factor (β) resulting from a kinetic impact. We simulate a variety of impactor shapes motivated by munitions ballistics and relevant spacecraft end-members at spatial and impact velocity scales relevant to laboratory settings and planetary defense. In total, we provide a statistical study to understand the role of mission parameters on the deflection efficiency resulting from kinetic impacts in order to inform future potential kinetic impactor missions designed for planetary defense.

2. Methods

2.1. Design of Experiments

We employ a design of experiments (DOE) architecture to study the role of mission parameters on the deflection efficiency parameters resulting from a kinetic impact. DOE is a mature methodology that is rooted in statistical modeling that estimates the individual effects of input parameters and their interactions on key output variables. DOE is more effective and efficient than the methodology of varying one factor at a time. First, a DOE approach requires fewer trials to sample the parameter space. Second, it accounts for both the individual and combined effects of input parameters. Lastly, DOE is more effective in finding the best setting to maximize yield (i.e., what combination of mission design parameters results in the largest deflection). See [Appendix](#) for more DOE details.

The DOE methodology was used via the statistical software package JMP® to design a test matrix that minimizes the number of hydrocode simulations required to understand the significance of a single mission design parameter on the deflection efficiency. In brief, JMP® allows for the specification of which effects are necessary to estimate given a number of runs. The DOE test matrix was designed to investigate the response of five mission parameters (impactor shape/mass/composition, impact velocity, and target strength) on three deflection efficiency observables (crater size, β , and ejecta distribution). Table 1 details 18 test cases defined by the DOE that were subsequently simulated using the shock physics code, CTH. Full details of the numerical modeling performed in CTH are provided in [Appendix A.2.1](#). The impactor masses and impact velocities were constrained to capture both laboratory and planetary defense scales. The impactor shapes included sphere, ogive, ring, plate, and a cone containing a solid or hollow nose. The impactor mass was constrained to 1 g and 500 kg, which represent a lab scale and a planetary defense scale (approximate mass of the spacecraft end-members discussed previously) impactor, respectively. Lastly, the impactor composition consisted of aluminum or copper. The impact velocity included 500 m s⁻¹ and 5 km s⁻¹, and the target consisted of nonporous homogeneous granite, where the cohesion strength was varied to achieve a strong, medium, and weak target (see [Table 2](#) for the full details of the target material parameters).

Table 1
Details of the DOE Test Matrix

Case	Impactor Shape	Mass (g)	Impactor Composition	Impact Velocity (m s ⁻¹)	Target Strength
1	Cone/ solid nose	5×10^5	Al	5000	Strong
2	Sphere	1	Cu	5000	Strong
3	Sphere	5×10^5	Al	500	Medium
4	Cone/hol- low nose	5×10^5	Al	500	Weak
5	Ogive	1	Al	5000	Weak
6	Ring	5×10^5	Cu	500	Weak
7	Plate	5×10^5	Cu	5000	Medium
8	Ring	5×10^5	Al	5000	Strong
9	Ring	1	Al	500	Medium
10	Ogive	1	Cu	500	Strong
11	Ogive	5×10^5	Cu	5000	Medium
12	Plate	1	Al	5000	Weak
13	Plate	1	Cu	500	Strong
14	Cone/hol- low nose	1	Cu	500	Medium
15	Cone/hol- low nose	5×10^5	Al	500	Strong
16	Cone/ solid nose	5×10^5	Cu	500	Weak
17	Cone/ solid nose	1	Al	500	Medium
18	Sphere	1	Cu	5000	Weak

Note. Refer to [Table 2](#) for target strength parameters.

2.2. Numerical Models

We use CTH to model the kinetic impacts of different impactor geometries onto asteroid-like surfaces. CTH is a multidimensional, multimaterial, large deformation, strong shock wave physics code developed by Sandia National Laboratories (McGlaun et al. 1990; Crawford 1999). It is an Eulerian code that exhibits a continuum representation of materials and also contains an adaptive mesh refinement (AMR) capability, which allows the user to select areas of high resolution to be generated within the mesh that result in better tracking of the shock wave and material interfaces. The development history and description of the models and novel features of CTH are described by McGlaun et al. (1990) and Trucano & McGlaun (1990). See [Appendix A.2.1 Numerical Model](#) for the full details of the CTH simulations inputs.

2.2.1. Impactor Geometry

This paper investigates six different impactor geometries: sphere, plate, ring, ogive, cone with a solid nose, and cone with a hollow nose ([Figure 2](#)). The morphology (shape) and composition (Al or Cu) of the impactors were motivated by experimental findings from previous works ([Ikeda et al. 2017](#)), munitions ballistics studies ([Harvey 1948](#); [Stefanopoulos et al. 2014](#)), and realistic impactor spacecraft end-members ([A’Hearn et al. 2005](#); [Schultz et al. 2010](#); [Cheng et al. 2018](#)). The simple impactor shapes (sphere, plate, and ring) were modeled using 2D AMR grids, which are less computationally expensive compared to their 3D counterparts. Performing 2D simulations with the simple impactor geometries allowed for efficient grid optimization at higher spatial resolution. The more complex

Table 2
Material Model Parameters Used for the CTH Simulations

Description	Impactor	Impactor	Target
Material	Al	Cu	Granite
EOS	ANEOS ^a	ANEOS ^a	Tillotson ^b
Strength model	SGL ^c	SGL ^c	BDL ^d
Density, ρ ($\frac{g}{cm^3}$)	2.785	8.930	2.65
Poisson ratio, γ	0.330	0.333	0.250
BDL Strength Parameters			
Shear strength at zero pressure, Y_{i0} (MPa)	1/45/90
Von Mises plastic limit, Y_m (GPa)	3.5
Coefficient of internal friction of intact rock	1.8
Coefficient of internal friction (damaged), μ_d	0.8
Brittle–ductile transition pressure (GPa)	2.56
Brittle-to-plastic transition pressure (GPa)	4.11
Brittle-to-plastic transition pressure at max failure strain (GPa)	8.22
Tensile strength (MPa)	–100
Strength at infinite pressure, Y_{inf} (GPa)	8.22
Damage at failure	0.7
Melting temperature, T_m (eV)	0.1600
SGL Strength Parameters			
Internal yield stress, Y_0 (MPa)	260	120	...
Max. yield stress, Y_M (MPa)	760	640	...
Internal shear modulus, G_0 (GPa)	28.6	47.7	...
Material constant, A ((Pa) ^{–1})	$6.52e^{-13}$	$2.83e^{-13}$...
Material constant, B ((eV) ^{–1})	7.15	4.38	...
Initial Gruneisen coefficient, γ_0	2.00	2.02	...
Melting temperature at constant volume, T_m (eV)	0.1051	0.1542	...

Notes.

^a Thompson & Lauson (1974).

^b Brundage (2013).

^c Taylor (1992).

^d The BDL parameters for granite remain unpublished and were obtained from the source code.

impactor shapes (solid and hollow-nosed cone and ogive) required 3D AMR schemes that consisted of slightly coarser spatial resolutions. It is important to note that previous resolution studies have shown that lower spatial resolutions can produce lower crater volumes and β values (Stickle et al. 2020). Here we define the spatial resolution based on how many cells per projectile/impactor radius (cpr) were used to represent the impactor shape (full details for each impactor are reported in Table A1). While the 3D meshes do not fully resolve the tip of the cone/ogive, the spatial resolution is approximately $cpr = 5$ for all cases as measured by the largest radius (r) contributing to the cone/ogive structure so that we do not expect any significant resolution effects when comparing the 2D to the 3D results (see Appendix A.2.1). All of the impactor structures considered had masses of either 1 g or 500 kg. The impactor geometries are shown in Figure 2 and Table A1.

The impactors investigated were modeled as nonporous aluminum or copper material using Sandia’s analytic equations of state (ANEOS; Thompson & Lauson 1974), which are widely used in impact simulations (Kipp & Melosh 1986; Benz et al. 1989; Pierazzo et al. 1997). ANEOS is a semianalytic model that is thermodynamically consistent because the pressures, temperatures, and densities are derived from the Helmholtz free energy (Pierazzo et al. 2008). Additionally, we used the Steinberg–Guinan–Lund (SGL) strain-rate constitutive model for “6061-T6 Aluminum” and “Copper,” applied, respectively, to each material-dependent equation of state (EOS), which are defined as standard options within CTH (Steinberg & Lund 1989; Taylor 1992; Hertel et al. 1995). The impactor input parameters are summarized in Table 2.

2.2.2. Target Material Model

In all of the impact scenarios investigated here, the target material was modeled as nonporous granite using the Tillotson EOS (Tillotson 1962; Brundage 2013) with the brittle damage with localized thermal softening (BDL) strength and damage model (Crawford & Schultz 2013; Schultz & Crawford 2016). The BDL model includes a pressure-dependent yield and brittle damage model based on the popular strength/damage model described by Collins et al. (2004), in which the plastic strain at failure increases across the brittle and ductile regimes and the yield strength of fully damaged material follows a Coulomb friction law. The BDL model also incorporates a pressure-dependent melt curve to determine thermal softening (Senft & Stewart 2009), as well as a statistical crack spacing model that accounts for localized frictional shear heating within cracks (Crawford & Schultz 2013; Schultz & Crawford 2016).

Previous works have shown that the target morphology (i.e., strength parameters) plays a dominant role in the cratering and ejecta processes proceeding a kinetic impact (Stickle et al. 2020). Therefore, we studied the influence of the impactor parameters (mass, impact velocity, geometry, and composition) on the cratering processes given different target morphologies by varying the cohesive strength of the intact material (Y_0). We defined the following varying degrees of granite strength: weak ($Y_0 = 1.0$ MPa), medium ($Y_0 = 45$ MPa), and strong ($Y_0 = 90$ MPa). Here BDL models the strength of the damaged material (Y_d) as

$$Y_d = \mu_D P_{\text{eff}}, \quad (1)$$

where μ_D is the coefficient of internal friction of the damaged material, and P_{eff} is the effective pressure. The target input parameters are summarized in Table 2. All simulations occurred in the strength-dominated regime so that no gravitational acceleration was considered in the simulations.

The cohesive strengths selected for this study are relatively strong compared to reports from recently visited asteroids, like Bennu and Ryugu, that exhibited cohesive strengths on the order of a few to a few hundred Pa (Scheeres et al. 2019; Sakatani et al. 2021). In general, targets containing higher-strength parameters result in lower cratering efficiency; therefore, simulations of high-strength material are more computationally efficient. We chose a range of relatively higher cohesive target strengths to improve computational efficiency, which allowed for the investigation of a larger parameter space while also remaining suitable for informing how target strength couples with impactor effects. Additionally, the tensile strength of the realistic geologic material also scales with cohesion. For

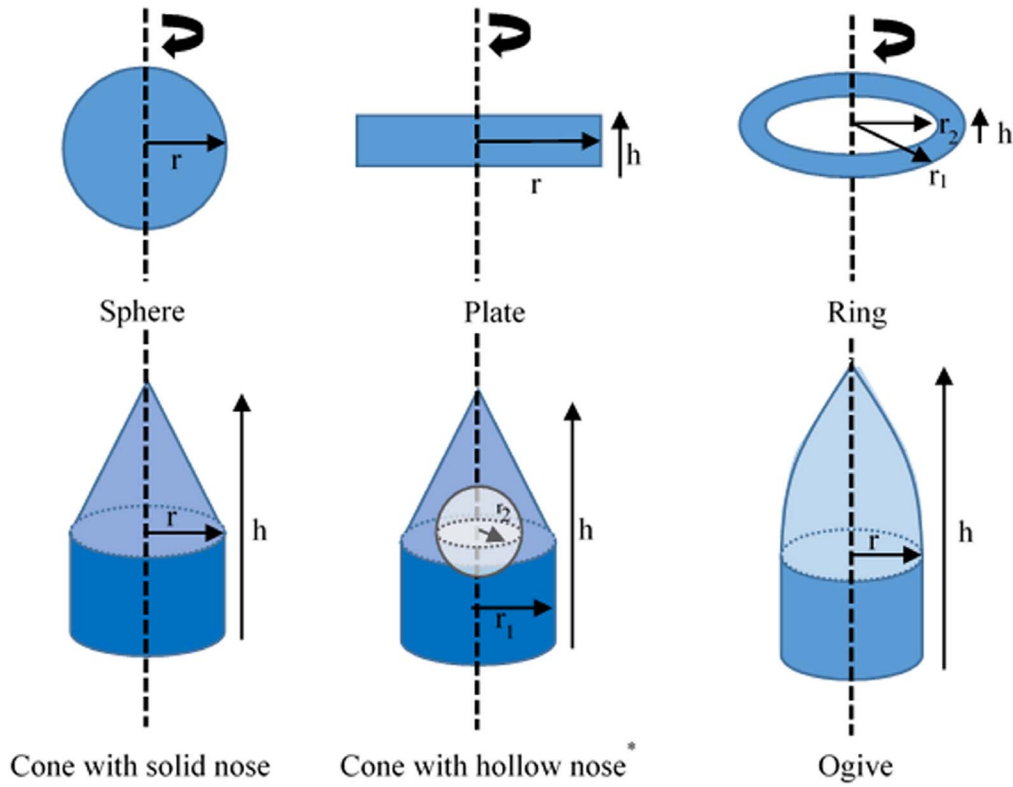


Figure 2. Schematic representation of the (top) 2D axisymmetric impactor structures and (bottom) 3D impactor structures investigated in this work. The limiting dimensions for each shape are labeled as r for the radius and h for the height. Refer to Table A1 for a full description of the impactor dimensions and resolutions for each test case. The asterisk indicates that the hollow nose is created by removing a sphere of material from the cone, resulting in the nose of the cone having variable thickness.

simplicity, we chose to vary only one strength parameter (cohesion) while keeping the tensile strength constant (-100 MPa) among each target. The effects of also varying the tensile strength are discussed in Appendix A.2.1 and are the focus of future work. We note that porosity in realistic asteroid target material will likely play a dramatic role in the resulting crater morphology, ejecta distribution, and momentum enhancement resulting from a kinetic impact (Barnouin et al. 2019; Raducan et al. 2019). In the presence of porosity, a large amount of the energy impinged on the target from the kinetic impact will be dedicated to pore crushing, which reduces both cratering and ejecta producing processes. While the role of target porosity is important in considering the deflection efficiency parameters resulting from realistic kinetic impactor applications (like DART), we chose not to include porosity in our target material to simplify the material models in order to focus on the effects of impactor geometry on deflection efficiency without overcomplicating the target material.

2.2.3. Ejecta Measurement

In CTH, the amount of momentum transfer from the impact as a function of time was calculated for each simulation. Ejecta material was defined as any material containing a void fraction greater than zero but less than 1, exhibiting positive upward velocity (positive y -direction in 2D and positive z -direction in 3D), and existing above the “ejecta plane.” We define the ejecta plane to occur at a distance of $+1\%$ of the target thickness above the impact plane (Figure 3) in order to avoid classifying material that is uplifted but remains attached to the crater lip as ejecta material.

The range of the mesh was conservatively limited in order to conserve computational resources. Therefore, some of the ejecta material left the grid before the transient crater was fully formed. In order to account for the exiting material, witness plates were placed at the grid boundary. These witness plates tracked the mass and velocity of each ejecta particle as it left the grid, so that the total ejecta momentum was

$$P_{\text{ejecta}} = \sum m_i v_i + \sum m_{i,e} v_{i,e}, \quad (2)$$

where m_i and v_i are the respective mass and velocity of the i th piece of ejecta material, and $m_{i,e}$ and $v_{i,e}$ are the mass and velocity of the i th piece of ejecta that has left the grid, respectively. The velocity used was the velocity component perpendicular to the impact plane (y -velocity for 2D and z -velocity for 3D cases). Finally, β was calculated following

$$\beta = 1 + \frac{P_{\text{ejecta}}}{P_{\text{impactor}}}, \quad (3)$$

where P_{impactor} was the initial impactor momentum (Bruck Syal et al. 2016; Heberling et al. 2017). In total, β depends on the initial momentum of the incoming impactor and the momentum of ejecta excavated during the formation of the transient crater, tracked in the direction of the intended deflection.

The transient crater resulting from impact was calculated using an algorithm that measured the depth and width of the crater by tracking the cells forming the boundary between the target material and void. The depth was measured from the impact plane to the maximum absolute value of the height location for the boundary cells, and the diameter was measured

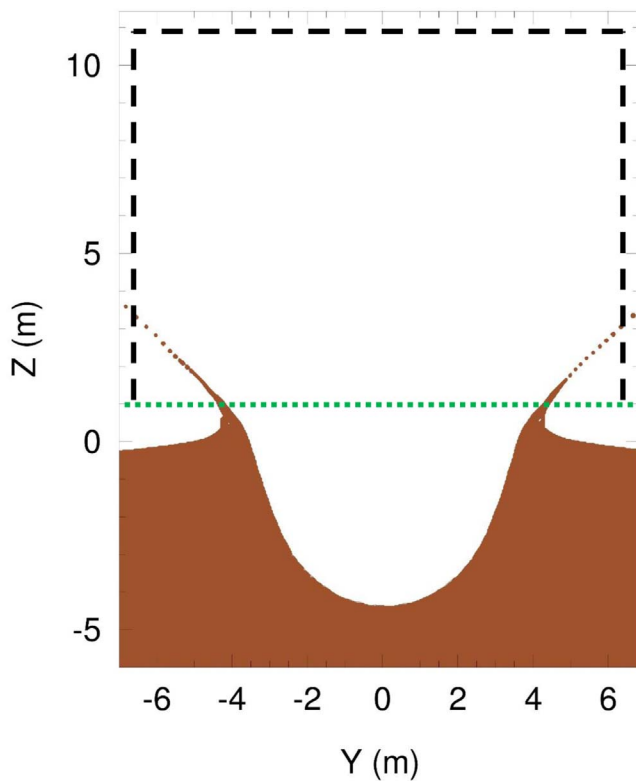


Figure 3. Schematic representation of the transient crater and resulting ejecta within CTH (case 2). The ejecta plane is shown as a green dotted line and placed above the impact plane at a distance of 1% of the target thickness. The witness plates are shown as black dashed lines and monitor the ejecta material leaving the grid.

as the distance between cells along the crater boundary profile that intersected the impact plane.

3. Results

3.1. CTH Results

This section details the results from our shock physics code modeling (CTH) applied to the 18 test cases identified by the DOE test matrix detailed in Table 1 and Appendix A.1. We investigated the role of five mission design parameters (impactor shape, impactor mass, impactor composition, impact velocity, and target strength) on three deflection efficiency observables (crater size, β , and ejecta distribution). The results are presented in two forms: Section 3.1 qualitatively details the results from CTH, and Section 3.2 quantitatively details the results from a statistical perspective by discussing the correlations among effects in terms of statistical p -values derived from the response surface developed within JMP[®].

3.1.1. Crater Size and Morphology

We investigated the influence of the five mission parameters on the crater size. Specifically, we considered six impactor geometries made of two different compositions (Al and Cu) impacting flat semi-infinite granite targets of varying strength in CTH (see Table 2 for full details). In all cases, bowl-shaped craters result. Figure 4 plots the crater volume, assuming spherical bowl-shaped craters, as a function of the impactor volume. Complimentary to this, Figures 5 and 6 illustrate the crater morphologies resulting from a select group of test cases. Specifically, Figure 5 shows the craters occurring after impact

from similarly shaped impactors (ogive or solid cone) into targets with varying strength, and Figure 6 shows the resulting craters from different impactor geometries into similar-strength targets at a constant impact velocity. All together, these figures indicate that the impactor mass and impact velocity have the greatest influence on the resulting crater volume.

It is well known that crater formation occurring from low-velocity impacts has phenomenological differences compared to craters formed from high-velocity impacts (Holsapple 1993; French 1998; Elbeshausen et al. 2009). When the impact velocity is significantly lower than the sound speed of the target material (i.e., 500 m s^{-1}), the momentum of the impactor drives the cratering process so that the resulting crater is only slightly larger than the impactor, and the impactor typically survives intact. In the case of hypervelocity impacts (i.e., 5 km s^{-1}), on the other hand, crater excavation results from an expanding shock wave initiated at the instant of impactor/target contact. This shock wave rapidly radiates outward through the target, resulting in permanent deformation effects producing a transient impact crater that is $10\text{--}20\times$ larger than the initial impactor (Elbeshausen et al. 2009).

All CTH simulations reported here occur in the “strength regime,” where the strength of the target surface is large compared to the stress exerted by the surrounding rock that makes up the target (Holsapple 1993). Therefore, at all impact velocities, when the target strength is held constant, scaling laws (that assume spherical impactors) indicate that the volume of the crater increases linearly with the volume of the impactor, its mass, and—at constant velocity—its energy (Holsapple 1993). All together, we see evidence of this in Figure 4, where the impactors with impact velocities of 500 m s^{-1} (filled symbols) have considerably smaller volumes than their hypervelocity counterparts (open symbols), but overall, the crater volume increased with impactor volume (when mass is held constant to 1 g or 500 kg). A few outliers emerged upon further examination of the 500 m s^{-1} impactors. In the case of the 1 g impactors (Figure 4(a)), case 14 (Cu cone with a hollow nose) resulted in a larger crater per unit volume in comparison to impactors with larger volumes that impact the same strength target material, such as cases 9 (Al ring) and 17 (Al cone with solid nose). Further, Figure 7(b) plots the results of cratering efficiency as a function of the normalized density and suggests that perhaps the projectile composition plays a role (i.e., copper outperforms aluminum). Together, this suggests that an impactor composition and geometry effect may occur when determining crater size at low impact velocities. Further, for the 500 kg impactors with 500 m s^{-1} impact velocities plotted in Figure 4(b), case 3 (Al sphere) had the largest impactor volume but resulted in a relatively smaller crater volume. Case 3 indicated that the sphere impactor may be less efficient than the cone-shaped impactor (case 15) in this regime. Further, Figures 5(a), (c), and (f) illustrate that the crater size for the low impact velocity impactors is roughly equivalent to the impactor volume and showcases that the impactor material (shown in gray) remained intact postimpact. These results are in line with traditional scaling laws developed considering vertical impacts (Holsapple 1993). Figures 5(b) and (d) illustrate that the target material’s cohesion strength may play a role, where weaker targets result in a deeper crater; however, the true effects of target strength are not easily visualized and must be interpreted statistically from the results detailed in Section 3.2.

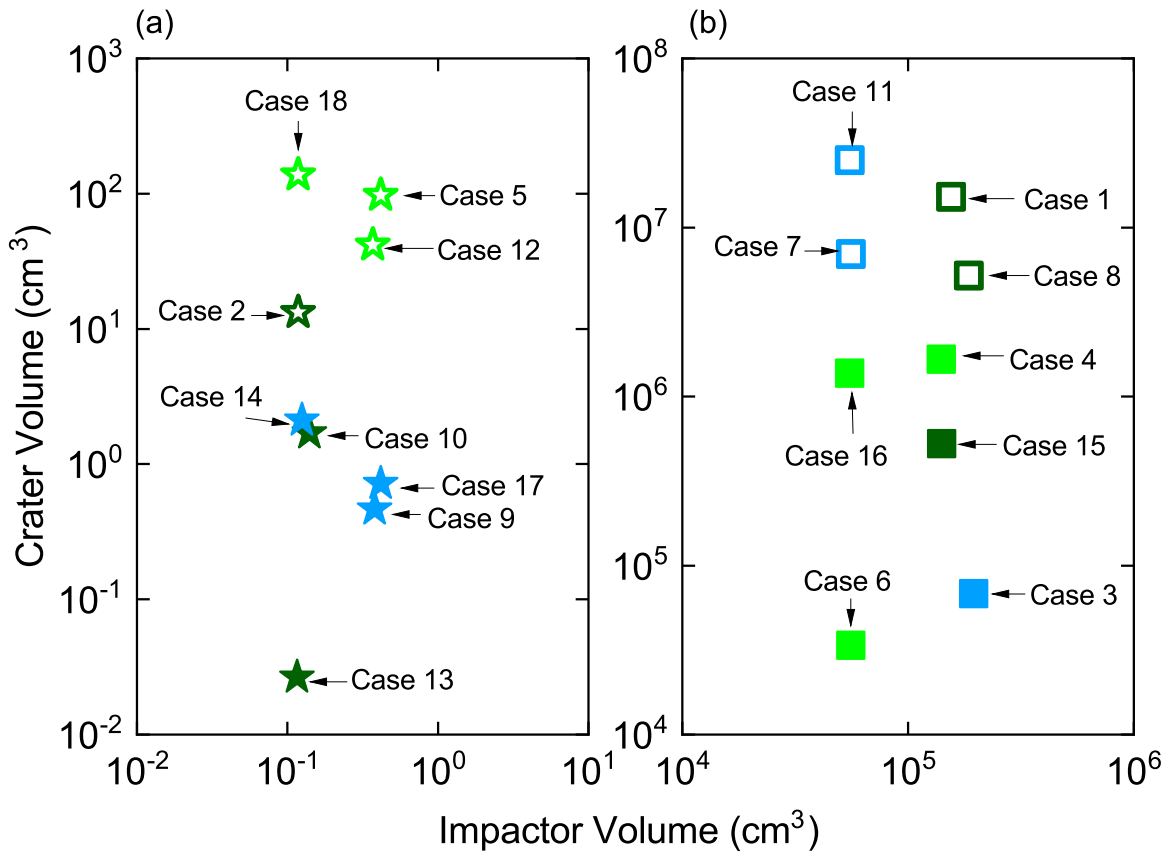


Figure 4. Crater volume as a function of impactor volume for (a) 1 g and (b) 500 kg impactors. The open symbols identify impactors with impact velocities of 5 km s^{-1} , and the filled symbols indicate impactors with impact velocities of 500 m s^{-1} . The target cohesion strength ranges from strong (dark green), to medium (blue), and to weak (bright green).

Figure 4 shows that the hypervelocity impactors exhibited entirely different magnitudes in crater size (because of quantitative differences in how the crater excavation occurs) but followed similar trends as their low impact velocity counterparts, where the crater size generally increased with impactor volume. Figures 5(b), (d), and (e) illustrate this further, where the resultant symmetrical transient craters were much larger than the initial impactor size. Notable exceptions to the strength scaling law shown in Figure 4 include case 18 (Cu sphere) for the 1 g impactors, which emerged as a highly efficient excavator compared to impactors with larger volumes, such as cases 5 (Al ogive) and 12 (Al plate). For the 500 kg impactor, case 8 (Al ring) contained the largest impactor volume (compared to the Al cone with a solid nose, Cu ogive, and Cu plate) but resulted in the lowest crater volume. This suggests that an impactor geometry effect may contribute to lower crater volumes in some unique cases.

Figure 6 shows the resultant transient craters at 10 ms postimpact from four different impactor geometries with constant impact velocities (5 km s^{-1}) into strong and medium strength targets. We see clearly that for the impactor geometries investigated here, a large geometry effect occurred on the crater morphology, where the ring (case 8) and plate (case 7) impactors produced much shallower craters compared to the solid cone (case 1) and ogive (case 11) impactors interacting with the same respective material. In all cases, symmetrical bowl-like craters result; however, we see evidence that the dimensions of the crater were influenced by the geometry of the impactor with constant masses. This is evidence that in the

strength regime, the cratering efficiency is dependent on the density ratio of the impactor.

3.1.2. Ejecta Mass–Velocity Distribution

In this work, we perform simulations to probe the full range of laboratory to deflection mission-relevant scales to understand the size dependence of the asteroid response to kinetic deflection. The simulations did not include gravity and occurred in the strength-dominated regime, where the applied strength model did not depend on the size scale. Therefore, when normalized by impactor mass/size, we found that the results for crater size (and β) are not dependent on the size scale of the impacts. Figures 7(a) and (b) plot the normalized results of the crater efficiency (ejecta mass (M)/impactor mass (m)) as a function of the normalized crater volume (crater volume/impactor volume) and normalized density (impactor density/target density). Figure 7(a) shows that cratering efficiency generally increases as a function of the normalized crater volume. Figure 7(b) shows that two distinct categories of projectiles emerge when plotted by the normalized density; $\rho_{\text{impactor}}/\rho_{\text{target}} \approx 1$ corresponds to the Al projectile, and $\rho_{\text{impactor}}/\rho_{\text{target}} \approx 3.5$ corresponds to the Cu projectile. Projectiles impacting weak targets generally result in high crater efficiency; however, we must rely on the statistical interpretation of the results presented in Section 3.2 to fully understand the asteroid response to the mission parameters of interest. In total, case 9 (Al ring) emerged as the most inefficient impactor in creating ejecta mass within the 1 g impactors with impact velocities of 500 m s^{-1} . Analysis of the

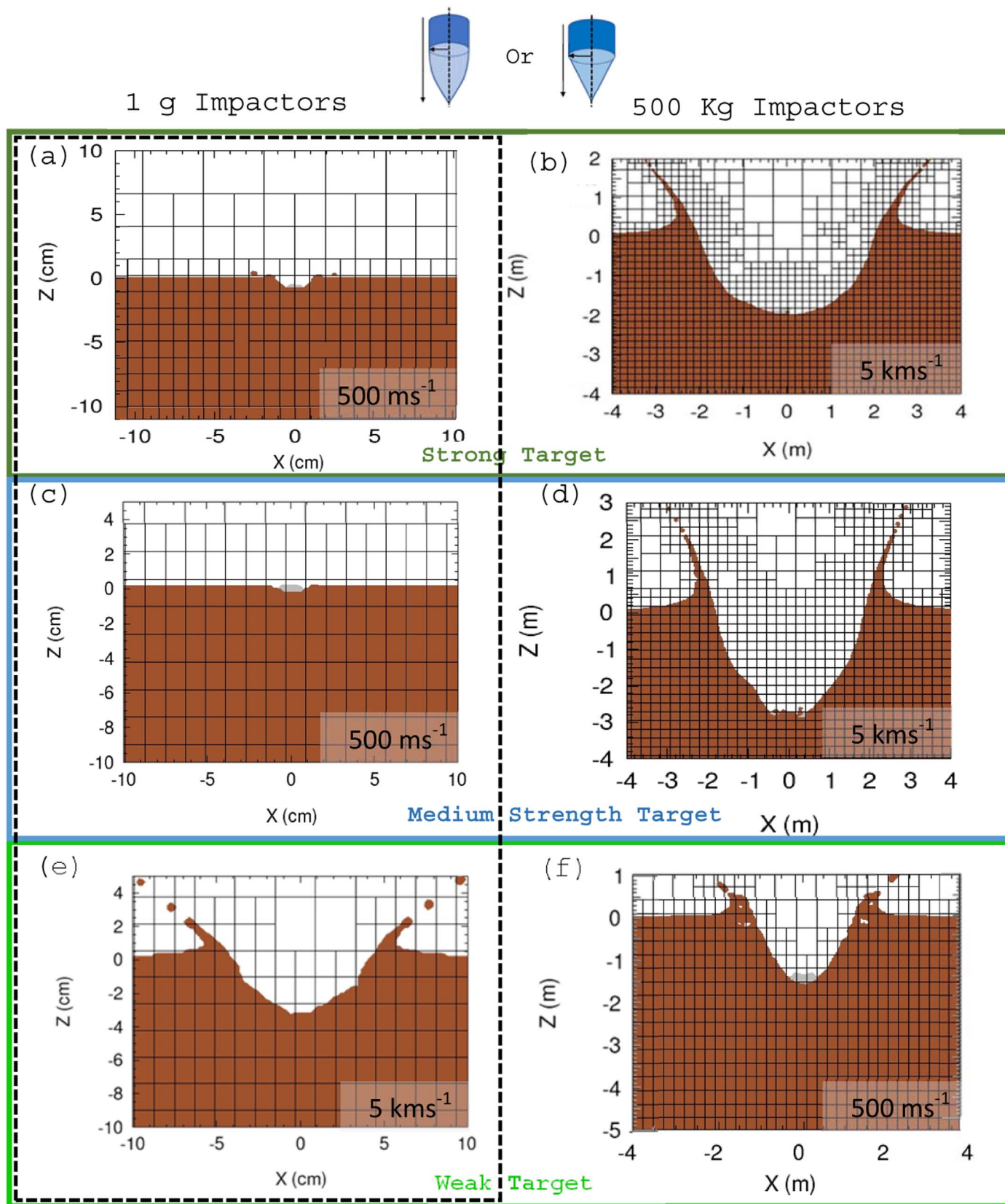


Figure 5. Crater profile for (panels (a), (c), and (e)) 1 g impactors at 1 ms post impact and (panels (b), (d), and (f)) 500 kg impactors at 10 ms post impact from similar impactor geometries (ogive or solid cone) but varying impact velocities. Note that the transient crater is fully formed 1 and 10 ms postimpact for the 1 g and 500 kg impactors, respectively. The target material is brown, and the impactor material is gray. The top dark green panels, middle blue panels, and bottom bright green panels illustrate craters resulting from strong, medium, and weak target material, respectively. The following cases and impact velocities are plotted: (a) case 10: ogive, 500 m s^{-1} ; (b) case 1: solid cone, 5 km s^{-1} ; (c) case 17: solid cone, 500 m s^{-1} ; (d) case 11: ogive, 5 km s^{-1} ; (e) case 5: ogive, 5 km s^{-1} ; and (f) case 16: solid cone, 500 m s^{-1} .

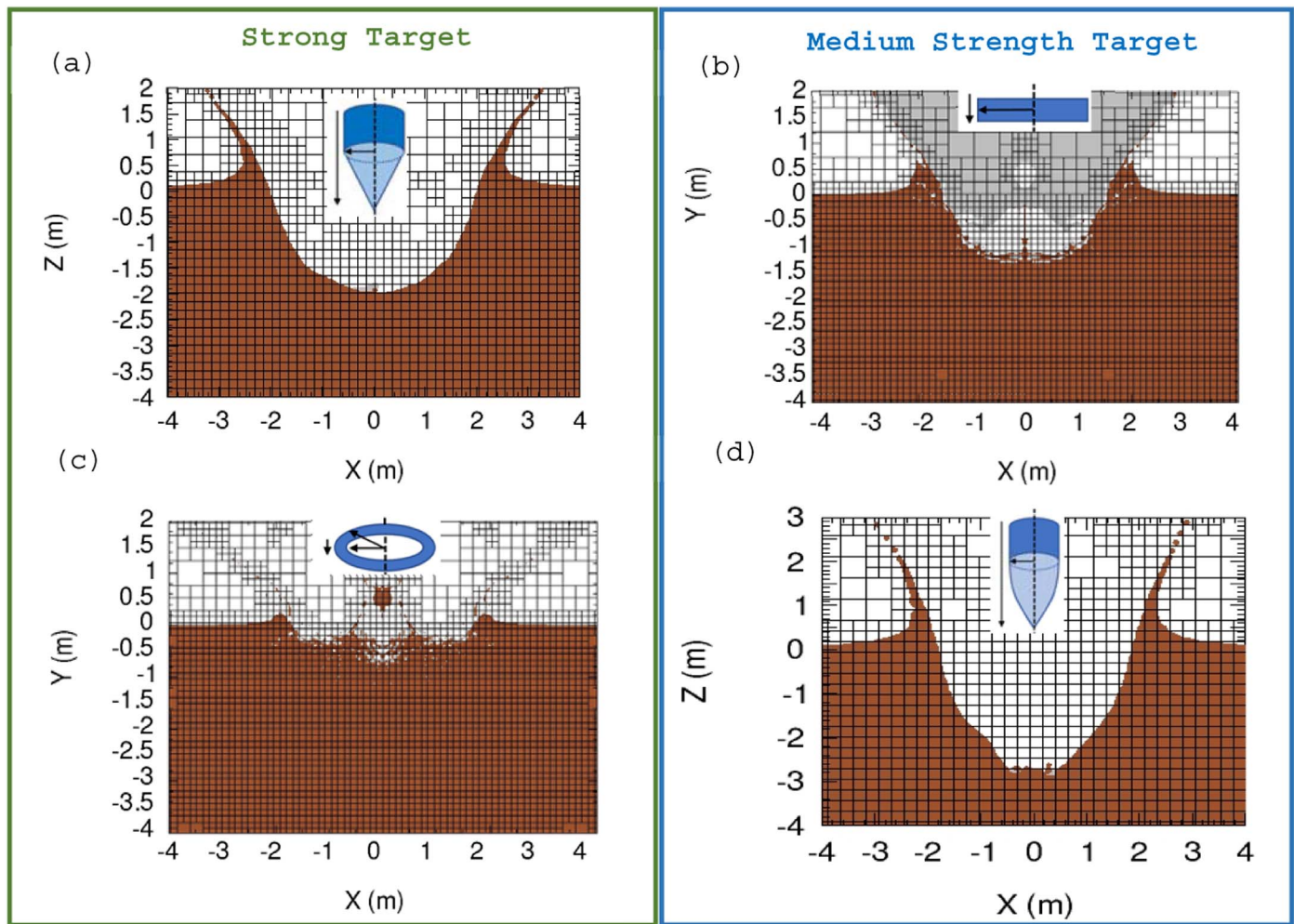


Figure 6. Transient crater profiles at 10 ms post impact from 500 kg impactors of differing geometry with impact velocities of 5 km s^{-1} into (panels (a) and (c)) strong and (panels (b) and (d)) medium strength target material. The following cases are plotted: (a) case 1: Al cone with solid nose; (b) case 7: Cu plate (note the gray ejecta plume consisting of target material); (c) case 8: Al ring; (d) case 11: Cu ogive.

500 kg impactors shows that the same impactor geometry (case 6: Cu ring) was responsible for producing the least normalized ejecta mass for the slower-moving impactors. Notably, cases 7 (Cu plate) and 8 (Al ring) emerged as the least efficient impactors at hypervelocity. Case 7 (Cu plate) contained a larger impactor volume and impacted a weaker target material compared to cases 1 and 8 (Cu sphere and Al ring); however, the copper plate resulted in significantly less ejecta mass. Additionally, cases 15 (Al cone with hollow nose) and 16 (Cu cone with solid nose) exhibited a rather large amount of ejecta mass compared to the other cases with similar parameters (500 m s^{-1} and 500 kg). Specifically, case 15 was run with a stronger target material and expected to result in less ejecta mass compared to the weaker and medium strength targets. Further investigation into case 15 (Al cone with hollow nose) shows that the crater contains a large lip of material that extends past the ejecta plane but does not detach at 10 ms post impact. Therefore, the slow-moving (ejecta velocity/impactor velocity < 0.001) excavated material forming the crater lip is erroneously classified as ejecta according to the definition of the ejecta plane given in this study. According to the definition for ejecta material, excavated material that remains attached to the target should not be classified as ejecta because it will not affect the deflection efficiency parameters of the kinetic impact.

For comparison, the result for case 15 is replotted in Figure 7 in dark green (case 15*) to show the effect of increasing the ejecta plane to 2% of the target thickness (20 cm). Adjusting the analysis this way results in a drop in the normalized ejecta mass by nearly an order of magnitude and is more in line with predictions from scaling laws. We note the same phenomena occurred in case 16, where the cone with the solid nose produced a large crater lip that extended beyond the nominal ejecta plane. This illustrates the importance of the definition of the ejecta plane when interpreting impact results. Particularly, it is clear here that the ejecta plane should not be a static value defined by the target thickness but rather should vary based on both the target size and strength and the impactor volume.

In order to better understand the role of projectile geometry on ejecta mass, we plot the distribution of the cumulative normalized ejecta mass as a function of its normalized velocity (ejecta velocity/impactor velocity). Figure 8 shows the normalized ejecta mass–velocity distributions by separating each panel by the target material strength: (a) strong, (b) medium, and (c) weak. The 1 g impactors are plotted as lines, and the 500 kg impactors are plotted as lines with symbols. Lastly, dotted and solid lines respectively distinguish impactors with impact velocities of 500 m s^{-1} and 5 km s^{-1} . Overall, impactors that interacted with weaker targets produced increasing amounts of cumulative ejecta mass. In

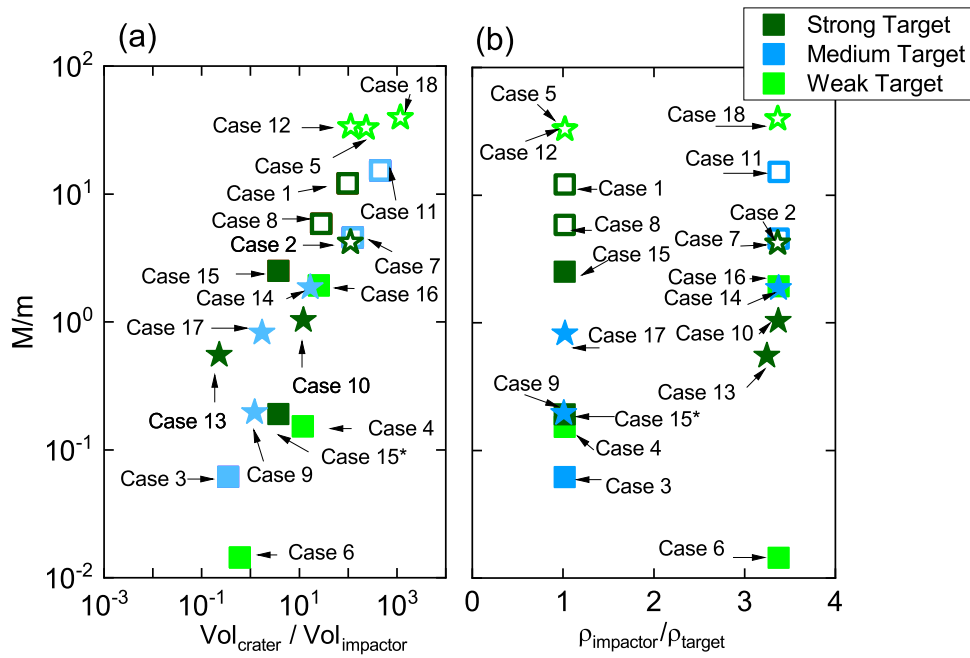


Figure 7. Cratering efficiency (total ejecta mass (M) normalized by the impactor mass (m)) as a function of (a) the normalized crater volume (crater volume/impactor volume) and (b) the normalized density (density of the impactor/density of the target) for 1 g (stars) and 500 kg (squares) impactors. The open symbols identify impactors with impact velocities of 5 km s^{-1} , and the filled symbols indicate impactors with impact velocities of 500 m s^{-1} . The target cohesion strength varies from strong (dark green), to medium (blue), to weak (bright green). Note that two separate results for case 15 are plotted; the dark green square labeled case 15 represents the total normalized ejecta mass with the traditional ejecta plane defined (1% of the target thickness), and the dark green square labeled case 15* represents the total normalized ejecta mass resulting with a larger ejecta plane defined (2% of the target thickness).

Figure 8(a), we see that for the impactors with impact velocities of 500 m s^{-1} , the Cu plate (case 13) produced an order of magnitude less ejecta mass moving at much slower speeds compared to the Cu ogive (case 10) and Al cone with a solid nose (case 15). The Al cone with the solid nose (case 15) had a large amount of slow-moving ejecta mass, which was likely material forming the crater rim. For the 5 km s^{-1} impactors, the Al cone with the solid nose (case 1) and Al ring (case 8) produced a larger amount of moderate- (normalized velocity $\sim 10^{-1}$) and high-velocity (normalized velocity ~ 0.5) ejecta material compared to the Cu sphere (case 2). All three of the hypervelocity impactors interacting with strong targets had similar ejecta velocity profiles/trends, with the lighter 1 g impactor (case 2) resulting in less ejecta material overall containing much slower velocities compared to its heavy counterparts (cases 1 and 8). In Figure 8(b), analysis of the slower-moving impactors interacting with medium strength targets shows that the Al cone with the solid nose (case 17) had distinctly different profiles from the other impactors, marked by a large amount of slow-moving ejecta material (ejecta velocity/impactor velocity $< 10^{-4}$). In contrast, the Al sphere (case 3), the Cu cone with a hollow nose (case 14), and the Al ring (case 9) had larger amounts of moderate-velocity ejecta material, with the Cu cone with a hollow nose (case 14) exhibiting the largest relative amount of moderate-high velocity ejecta. The hypervelocity impactors interacting with medium strength target material resulted in marked contrasts. The Cu plate (case 7) produced nearly an order of magnitude less ejecta material, partially because of the lack of a large crater lip. Interestingly, the plate did produce a larger amount of moderate-velocity ejecta in comparison to the Cu ogive (case 11). Figure 8(c) plots the results of the impactors interacting with weak targets. In this target strength regime, impactors with impact velocities of 500 m s^{-1} resulted in distinctly different ejecta mass-velocity distributions from one another, which may be evidence for an impactor

geometry effect. The Cu ring (case 6) created the least amount of cumulative ejecta mass. Additionally, the ejecta that was created has slower velocities (normalized ejecta velocity $< 10^{-4}$), while the Al cone with a hollow nose (case 4) and the Cu cone with a solid nose (case 16) contained populations of much faster-moving ejecta. In sharp contrast to this, the fast-moving impactors exhibit much more similar ejecta mass-velocity distribution profiles. The Al plate (case 12) resulted in a higher amount of fast to very fast moving ejecta (normalized ejecta velocity $10^1 < \times < 10^0$) but had a smaller amount of moderate-velocity ejecta material compared to the Cu sphere (case 18) and the Al ogive (case 5). This is similar to the trend observed by the Cu plate (case 7) impacting moderate strength target material at hypervelocity.

Overall, we see some evidence of geometry effects occurring in the normalized ejecta mass-velocity distributions for the impactors with impact velocities of 500 m s^{-1} . In particular, flatter impactors containing smaller volumes (i.e., case 13: Cu plate; case 6: Cu ring) produce a smaller amount of ejecta mass overall that exhibited distinctively slower ejecta velocity profiles. The cone with a solid nose (cases 15, 16, and 17) consistently exhibited a large amount of slow-moving ejecta material when impacting all of the target material types, which was indicative of the formation of excavated material that may remain attached to a large crater lip. Evidence for impactor geometry effects on the ejecta is not as apparent for impactors with impact velocities of 5 km s^{-1} . In these cases, the normalized ejecta mass-velocity distribution profiles showed some convergence. Similar to the slow-moving impactors, the ogive impactors (cases 5 and 11) exhibited a large amount of slow-moving material, which was consistent with excavated crater material that formed a large crater lip. We see that flat impactors with relatively smaller volumes (case 8: Al ring; case 7: Cu plate; case 12: Al plate) produced the smallest magnitude of ejecta mass, and all contained a larger amount of moderate-

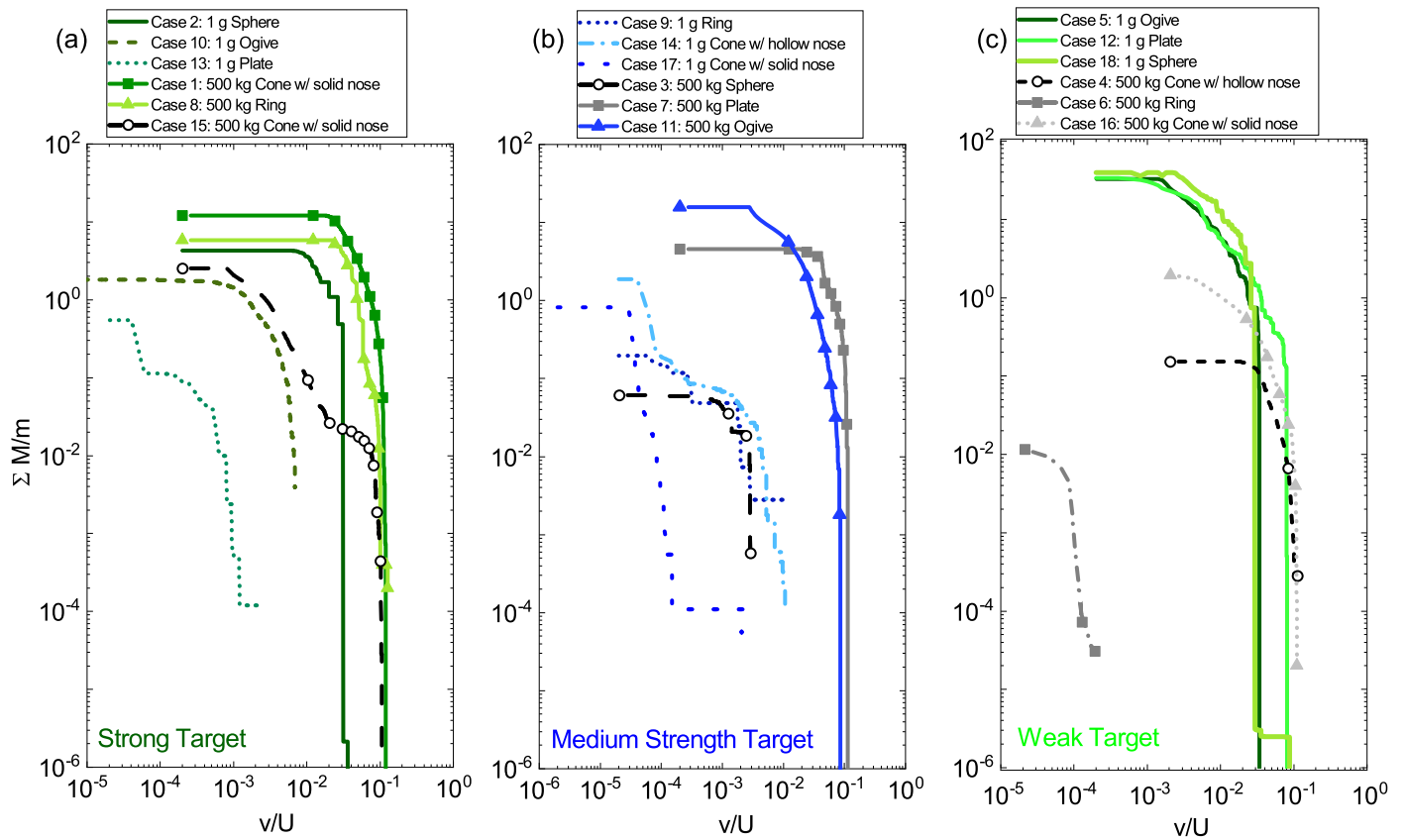


Figure 8. Distribution of cumulative normalized ejecta mass (ejecta mass (m)/impactor mass (M)) as a function of normalized ejecta velocity (ejecta velocity (v)/impact velocity (U)) into (a) strong, (b) medium, and (c) weak target material. The 1 g impactors are plotted with lines and symbols, and the 500 kg impactors are plotted as lines (no symbols). The mass-velocity distributions represent 1 ms post impact for the 1 g impactors and 10 ms post impact for the 500 kg impactors because those time intervals reflect the completion of transient crater excavation. Impactors with impact velocities of 500 m s⁻¹ and 5 km s⁻¹ take the form of segmented (dashed or dotted) and solid lines, respectively.

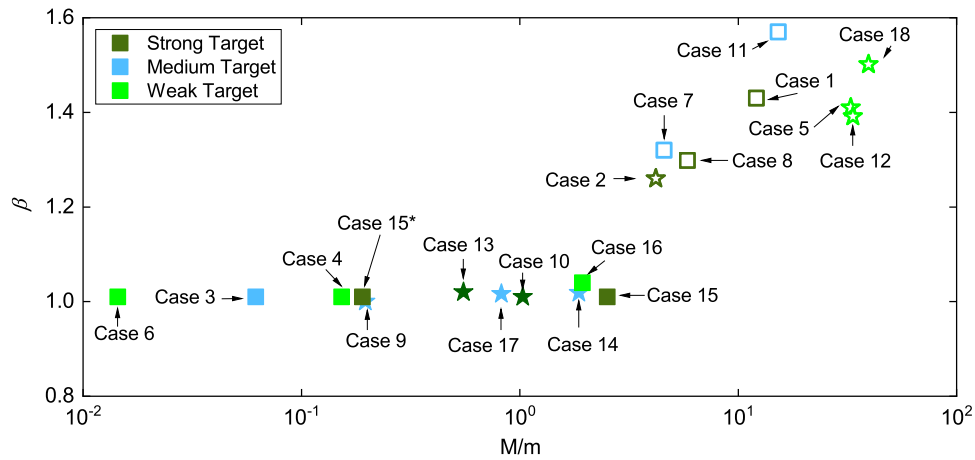


Figure 9. Momentum enhancement factor (β) as a function of the normalized ejecta mass (total ejecta mass (M)/impactor mass (m)). The stars represent 1 g impactors and the squares 500 kg impactors; filled and open symbols represent impact velocities of 500 m s⁻¹ and 5 km s⁻¹, respectively.

velocity ejecta material compared to the other impactor geometries that had larger volumes. Ogives and cones with a solid nose consistently produced the most cumulative normalized ejecta mass at all impact velocities.

3.1.3. Momentum Enhancement Factor (β)

An important metric for understanding the efficiency of a kinetic impactor scenario is measuring the amount of momentum transferred to the target by the impact. For a low-

velocity impact, the ejecta momentum is negligible so that Equation (3) predicts $\beta \sim 1$. Figure 9 confirms such an approximation, where all 500 m s⁻¹ cases exhibit β close to unity, stemming from the lack of ejecta momentum following impact. In a high-velocity impact, the change in momentum of the target can be amplified by contributions from the ejecta momentum that act as an additional thruster. In Figure 9, all cases pertaining to hypervelocity impacts exhibit β above unity. As a general trend, impacts into weaker targets result in

Table 3
Results from the Significance Testing Using the JMP Statistical Software

Mission Parameter	<i>p</i> -value				
	Crater Depth	Crater Width	Ejecta Mass	Ejecta Momentum	β
Impactor mass	<0.001	<0.001	<0.001	<0.001	0.125
Impact velocity	<0.001	<0.001	<0.001	<0.001	<0.001
Impactor geometry	0.080	0.167	0.111	0.131	0.141
Impactor composition	0.990	0.051	0.292	0.102	0.254
Target strength	0.225	0.101	0.034	0.252	0.342

Note. The nonnormalized results are presented here. Statistically significant *p*-values are shown in bold.

more ejecta mass and larger β values. Overall, cases 11 (Cu ogive), 18 (Cu sphere), and 1 (Al cone with a solid nose) result in the largest β of the impactors sampled. Inspection of the ejecta mass–velocity distribution of case 11 (Cu ogive) plotted in Figure 8(b) shows a small amount of very fast moving ejecta (normalized ejecta $>10^{-1}$) in addition to a large amount of ejecta material with moderate velocity that contributes significantly to enhancing β . For case 18 (Cu sphere), it is the contribution of ejecta material with moderate velocity that contributes the most to β .

3.2. DOE (JMP) Results

The JMP software package was used to evaluate the statistical significance of the five chosen mission parameters (impact velocity, impactor mass, impactor composition, impactor geometry, and target strength) on crater size, ejecta mass and momentum, and β . We determine a probability value (*p*-value) to determine the significance of our results in relation to the null hypothesis (i.e., there is no relationship between the two variables under study). Note that the level of statistical significance of the *p*-value lies between zero and 1, where the smaller the *p*-value, the stronger the evidence that one should reject the null hypothesis (i.e., there is no relationship between the two variables under study). Table A2 lists the results used from each CTH simulation to fit and determine a response surface to evaluate the importance of each parameter on the final crater size, ejecta properties, and final momentum enhancement. Since normality is an important assumption in order to derive *p*-values, we imposed a Box–Cox transformation on the initial input data so that it closely resembled a normal distribution Box & Cox (1964). This was necessary in order to perform the desired statistical analysis on the data set because normality is an important assumption for significance testing. This transformation improved the predictive power of our models because it removed white noise and normalized the errors (see Appendix A.2 for further detail). In all cases, the threshold of significance was $p \leq 0.05$. The results from the significance testing are summarized in Table 3, where the mission parameters that are statistically significant for determining the outcome of a deflection efficiency observable are indicated with bold numbering.

Figures A2 and A3 plot the results of the Box–Cox transformation of the actual versus predicted values from the JMP-derived fit model for the crater depth and width, ejecta mass and momentum, and momentum enhancement factor. Figure A2 and Table 3 show that impactor mass and velocity strongly influence both the crater depth and width. The impactor geometry, composition, and target strength do not emerge as statistically significant indicators for influencing crater size under the conditions studied. We note that others

have shown the strong influence of target strength on cratering and hypothesize that perhaps the target strength was not varied enough to truly capture the influence of target strength on the crater size (Bruck Syal et al. 2016; Raducan et al. 2019).

Figure A3 plots the results of the Box–Cox transformation of the actual versus predicted values from the JMP-derived fit model for the total ejecta mass and ejecta momentum. The figure and corresponding *p*-values (Table 3) show that the impact mass, velocity, and target strength are statistically significant predictors for the resulting ejecta mass following impact. For the total ejecta momentum, however, only the impactor mass and velocity exhibit $p \leq 0.05$ and are therefore the only two parameters that are correlated with predicting the ejecta momentum resulting from impact. This finding suggests that an enhancement in ejecta mass that occurs from weaker targets does not necessarily come with an enhancement in the total ejecta momentum.

Lastly, Figure A4 plots the results of the *p*-values and Box–Cox transformation of the actual versus predicted values from the JMP-derived fit model for β . Together, Figure A3 and Table 3 show that impact velocity dominates the response. This is an unsurprising result because of the large range between laboratory-scale and planetary defense-scale impact velocities, so it is expected that this parameter would have the largest effect in the analysis. Although the *p*-values for the impactor mass and shape have *p*-values slightly above the established threshold of significance ($p > 0.05$), the fact that they are relatively small indicates the possibility of a correlation that may emerge with further testing.

In total, the impactor mass and impact velocity dominate the response of mission design parameters on the deflection efficiency observables. The role of impactor geometry and composition does not emerge as statistically significant in this study; however, the projectile geometry results do exhibit low *p*-values that motivate future work into further understanding the role of projectile geometry on hypervelocity impacts.

4. Discussion

Here we investigate five mission parameters (impactor mass, impact velocity, impactor geometry, impactor composition, and target strength) to understand their role in the crater size, ejecta mass–velocity distribution, and momentum enhancement factor resulting from a kinetic impact. The results of 18 CTH kinetic impact simulations were used as inputs to a statistical model to provide support for understanding which mission parameters are related to the post impact factors of interest. In all cases, the impact velocity was the most statistically significant parameter in determining crater size, ejecta distribution, and β . The impactor mass emerged as a statistically significant parameter

in determining the crater size and ejecta properties but was nonsignificant for determining β , because β is normalized by it, and there is no size-scale dependence of the impact outcome in the strength regime. The impactor geometry and composition emerged as nonsignificant mission parameters for determining all of the post impact factors. Finally, the target strength had a statistically significant correlation to the ejecta mass but a nonsignificant relationship to the crater size, ejecta momentum, and β . Previous work has shown that target strength strongly influences the asteroid response to kinetic deflections (Bruck Syal et al. 2016; Raducan et al. 2019). While we report that the target strength emerges as statistically significant for influencing the ejecta mass, the nonsignificant relationship with the other response parameters does not imply that there is no correlation between them. The DOE study did not capture a relationship between the target strength and crater size and β because of how the target strengths were defined in CTH. The results indicated that varying the shear strength of the target from 1.0 to 90 MPa while keeping all other parameters in the damage model constant resulted in granite targets that behaved quite similarly to one another. In this paper, the cohesion (shear strength at zero pressure) was varied (1.0–90 MPa), but the tensile strength was kept constant at a very high value (–100 MPa). A more realistic target material would be achieved by varying the tensile strength to be comparable to the cohesion and is the subject of future work; see SI S.1.3 for further details.

The results from the CTH investigation of the effect of mission parameters on the crater size resulting from a kinetic impact showed strong evidence that the impactor mass and impact velocity were statistically significant in affecting the resulting crater size. This result was in line with previously derived theory and scaling laws that described kinetic impactor processes (Holsapple 1993; Holsapple & Housen 2012; Bruck Syal et al. 2016). The statistically derived p -values indicated that the impactor geometry, composition, and target strength were nonsignificant, meaning that we failed to reject the null hypothesis (that there is no relationship between the variables under study). Although these parameters were classified as nonsignificant, we note that the impactor geometry and composition did have p -values that were only slightly larger than our defined threshold of significance; therefore, further investigation may show a relationship between impactor geometry and composition on the impact crater. In particular, Figure 6 illustrates how impactors with larger volumes (i.e., ring and plate) formed shallower craters compared to impactors exhibiting the same mass and impact velocity.

Our study shows evidence that the impactor mass, impact velocity, and target strength are three mission parameters that were statistically significant for predicting the ejecta properties resulting from a kinetic impact. The impactor mass and velocity exhibited $p < 0.001$, which showed strong evidence for rejection of the null hypothesis, but it does not necessarily mean that they are correlated (i.e., that the alternative hypothesis is true). Figure 7 shows that the total ejecta mass can span up to 3 orders of magnitude when the impactor mass is held constant, but other mission parameters are varied (mainly impact velocity, impactor geometry, and target strength). Figure 7 does highlight the role of impact velocity on ejecta mass, where all impactors resulting in hypervelocity impacts produce significantly more ejecta mass because of phenomenological differences in the crater excavation process.

Interestingly, the target strength was a significant predictor for the total ejecta mass but not the total ejecta momentum. This suggests that the velocity distribution of the ejecta was unaffected by the target strength. Note, however, that more realistic target properties should be studied to fully understand these effects. Previous experimental kinetic impact studies (Ikeda et al. 2017) have suggested that the impactor geometry may influence the ejecta velocity distribution. We do not see strong statistical evidence that supports this; however, as discussed in Section 3.1.2, Figure 8 showed some evidence of geometry effects occurring in the normalized ejecta mass–velocity distributions for the impactors with impact velocities of 500 m s^{-1} . In particular, flatter impactors containing smaller volumes produced a smaller amount of ejecta mass overall that exhibited distinctively slower ejecta velocity profiles.

The impact velocity emerged as the only mission parameter that was statistically significant in predicting the β resulting from a hypervelocity impact. This was because of the quantitative differences in the excavating processes at play, where the input momentum of the impactor drives “slow” impacts (occurring below the sound speed of the target material), and the propagating shock wave drives excavation in hypervelocity impacts. The hypervelocity cases that resulted in the highest β include cases 1 (Al cone with a solid nose), 11 (Cu ogive), and 18 (Cu sphere). All of these impactors produced larger craters per unit volume compared to other impactor shapes impacting the same target at the same velocity (Figure 4). Cases 1, 11, and 18 all exhibited a small (normalized ejecta mass $< 10^{-6}$) amount of very fast moving (normalized ejecta velocity $> 3 \times 10^{-2}$) ejecta, and the majority of the ejecta mass exhibited moderate (normalized ejecta velocity $1 \times 10^{-2} < x < 3 \times 10^{-2}$) velocities, where excavated material did not remain attached to the crater lip.

5. Conclusions

In order to inform future studies of more efficient kinetic impactors, we performed a simulation study in CTH to understand the role of mission parameters (impactor mass, impact velocity, impactor geometry, impactor composition, and target strength) on post impact factors (crater size, ejecta mass–velocity distribution, and momentum enhancement factor). These post impact factors have been established as key observables for understanding the deflection efficiency resulting from a kinetic impact. We used a DOE approach to test multiple mission parameters concomitantly and employed a statistical analysis to understand the significance of each mission parameter on the post impact factor of interest.

We found that the impactor mass and velocity are statistically significant for predicting the crater size; the impactor mass, velocity, and target strength are significant for predicting the ejecta properties; and only the impact velocity is significant for predicting the momentum efficiency factor (β). The lack of statistical significance of the other mission parameters applied to a post impact factor does not mean that the two are uncorrelated. It simply means that we fail to reject the hypothesis that there is no relationship between the two variables under study (null hypothesis), and that more investigation is required (i.e., consider more impactor geometries, compositions, etc.). The analysis and discussion provided in Section 3.1 shows evidence for an impactor geometry effect occurring in the crater depth, where impactors with larger surface area (rings, plates) result in much shallower craters.

Overall, we do see some qualitative evidence of geometry effects occurring in the ejecta mass–velocity distributions for the impactors with impact velocities of 500 m s^{-1} . Again, flatter impactors containing large surface areas (i.e., case 13: Cu plate; case 6: Cu ring) produced a smaller amount of ejecta mass overall that exhibited distinctively slower ejecta velocity profiles. The hypervelocity impactors all exhibited similar ejecta mass–velocity distribution profiles, evidence for a lack of an impactor geometry effect on the ejecta. Lastly, impact velocity was the only statistically significant mission parameter for predicting the momentum enhancement factor (β). At hypervelocity, the cone with a solid nose, ogive, and sphere all resulted in large β ; however, a clear favorable geometry was not apparent because these geometries exhibit quite a large variance over the variable ranges tested in this work.

The authors acknowledge funding from the Johns Hopkins University Applied Physics Lab through both a 2021 Civil Space IRAD grant and a 2021 JANNEY Energize grant. M.E. D. also acknowledges funding from NASA (grant No. 80NSSC22K0242). The authors would also like to thank those who volunteered their time participating in discussions: Terik Daly, Dawn Graninger, and Patrick King.

Appendix A

A.1. Methods

This section provides details of the motivation for this study, a description of the statistical DOE methodology used to define the test matrix and perform the analysis, and an overview of the numerical modeling. In brief, we numerically investigate the role of mission design parameters, such as impactor geometry, on the deflection efficiency resulting from a kinetic impact. We use a statistical methodology to design our test matrix that allows for the minimization of computationally expensive simulations while allowing a quantitative metric for understanding the significance of each mission design parameter on the outcome.

A.1.1. Motivation

The motivation for the impactor shapes investigated in this work comes partially from studies of munitions ballistics and previous experiments with ballistic pendulums paired with light gas guns, which offer some insight into the role of impactor geometry in cratering and momentum enhancement. It is well known in munitions ballistics that the ballistic properties of penetrating impactors (i.e., mass, nose contour, and the addition of jackets that protect against friction from the barrel and help control deformation at impact) lead to different effects determined by the interaction between the impactor and target. In this case, increased damage is often achieved through deformation of expanding bullets upon impact, which substantially enhances the energy transfer to the target and increases the crater’s diameter. Although the impactor momentum of a bullet is approximately 5 orders of magnitude smaller than what would occur at planetary defense scales, lessons learned from munitions ballistics may be applied to designing kinetic impactors for planetary defense. Namely, it may be possible to optimize the rate of energy transfer to the target material through tuning the shape (i.e., frontal surface area) of the impactor.

A.2. DOE

The DOE approach allows multiple input parameters to be evaluated to determine their effect on an unknown response. Multiple inputs are evaluated simultaneously to identify important interactions that might otherwise be missed in more traditional parameter sweeps (i.e., where one parameter is changed at a time). All possible combinations of parameters may be investigated or only a subset. The DOE is especially well suited for investigations where more than one input factor is suspected of influencing an output (like impactor shape and composition) or to confirm suspected input/output relationships and develop a predictive equation suitable for performing what-if analysis.

Traditional methods of parameter space exploration involve picking a “nominal” case and varying parameters one at a time to determine responses. This requires many runs and may miss meaningful relationships that occur between variables within the parameter space that affect the measured response (for example, a combination of impactor shape coupled with target strength could define the role of impactor geometry on crater formation). On the other hand, DOE uses well-studied statistical methods (Goos & Jones 2011; Jones & Nachtsheim 2011; Santner et al. 2014) to determine the dominant parameters causing variance within data while also minimizing the number of runs to cover large parameter spaces; it also provides information about the most statistically significant results. This method also allows a multidimensional exploration of responses within limited resources, which is quite relevant for the study detailed here.

The DOE is a branch of applied statistics that allows for planning, analyzing, and interpreting controlled tests to evaluate the factors that control the value of a parameter. We use it to design a test matrix with a minimally optimized number of runs that allows for the interpretation of the effects of the mission design parameter of a kinetic impactor on the resulting deflection efficiency observables. Minimizing the test matrix is crucial for performing hydrocode studies that require significant computational resources. Statistical significance testing (p -values) is applied to quantitatively interpret the results. This analysis requires that the errors are normally distributed. In order to accomplish this, we perform a Box–Cox transformation on our results so that it closely resembles a normal distribution. The Box–Cox transformation takes the following form:

$$w = \begin{cases} \log(y) & \text{if } \lambda = 0 \\ (y^\lambda - 1)/\lambda & \text{otherwise} \end{cases},$$

where w is the transformed variable, y is the target variable, and λ is a fitted parameter that provides the best approximation for the normal distribution of the response variable. The optimal value is $\lambda = 1$, which indicates that the data are already normally distributed (so the transformation is not needed).

A.2.1. Numerical Model

CTH has been extensively benchmarked and validated against both laboratory-scale high-velocity impact experiments and other numerical shock physics codes (Spheral, iSALE, RAGE, PAGOSA) on the ability to reproduce the crater morphology, the corresponding ejecta material distribution (velocity and size), and β resulting from high-velocity impacts (Grady & Winfree 2001; Pierazzo et al. 2008; Stickle et al. 2020). In general, these

Table A1
CTH Test Matrix Overview Detailing Limiting Impactor Length Scales and Grid Resolutions for Each Test Case

Case	Grid Geometry	Impactor Shape	Mass (g)	Impactor Limiting Length (i.e., radius (r)) (cm)	Resolution cppr = 5 (cm cell ⁻¹)
1	3DR	Cone/solid nose	5×10^5	$h = 40.00, r = 14.41$	2.00
2	2DC	Sphere	1	$r = 0.30$	0.06
3	2DC	Sphere	5×10^5	$r = 35.36$	7.20
4	3DR	Cone/hollow nose	5×10^5	$h = 40.00, r = 14.41, r_d = 14.00$	2.00
5	3DR	Ogive	1	$h = 0.5, r = 0.01$	0.002
6	2DC	Ring	5×10^5	$h = 10, r_1 = 90.69, r_2 = 100.00$	1.80
7	2DC	Plate	5×10^5	$h = 10.00, r = 42.15$	2.00
8	2DC	Ring	5×10^5	height = 10, $r_1 = 90.10, r_2 = 118.40$	2.00
9	2DC	Ring	1	height = 0.35, $r_1 = 0.34, r_2 = 0.68$	0.07
10	3DR	Ogive	1	$h = 0.5, r = 0.002$	0.02
11	3DR	Ogive	5×10^5	$h = 45, r = 0.13$	2.00
12	2DC	Plate	1	$h = 0.1, r = 1.085$	0.02
13	2DC	Plate	1	$h = 0.10, r = 0.60$	0.02
14	3DR	Cone/hollow nose	1	$h = 0.50, r = 0.003, r_d = 0.002$	0.02
15	3DR	Cone/hollow nose	5×10^5	$h = 40, r = 13.72, r_d = 13.00$	2.60
16	3DR	Cone/solid nose	5×10^5	$h = 45, r = 13$	2.00
17	3DR	Cone/solid nose	1	$h = 0.5, r = 0.13$	0.20
18	2DC	Sphere	1	$r = 0.30$	0.06

previous works show that the variability in the prediction of momentum enhancement is highly resolution-dependent, requiring higher resolutions to converge compared to the crater size. Additionally, the choices of the strength model and material porosity have large effects on the resulting crater size and β compared to the variation among codes, emphasizing the important role that the target morphology plays in the kinetic impact response, the details of which are provided below.

This numerical study was designed to quantify the effects of mission parameters on crater size, ejecta mass–velocity distribution, and momentum enhancement. We divide our study into two parts by considering impactors of laboratory-scale (1 g) and planetary defense-scale (500 kg) masses. This distinction provides insight into the role of the impactor’s spatial scale on the deflection efficiency parameters resulting from a kinetic impact. We performed most of the simulations in two dimensions with an axially symmetric geometry (2DC). Here the computational domain was modeled as a half-space, with the symmetry axis located at the y -axis. Some of the more complex impactor geometry shapes (solid/hollow-nosed cone and ogive) required that the simulations be performed in three dimensions. For these test cases, we used a 3D rectangular geometry (3DR), which uses Cartesian coordinates (x, y, z). In the 3DR geometry, the full 3D Euclidean space is modeled. For this work, we rely on previous CTH convergence studies to appropriately set the spatial resolution of the grid using an AMR scheme while balancing finite computational resources (Stickle et al. 2020). In impact cratering simulations, the spatial resolution is reported in terms of cppr and representative of the resolution corresponding to the most highly refined mesh. We select a cppr $\cong 5$, which corresponds to a resolution (cm cell⁻¹)

ranging from 5.3 to 12.0 cm cell⁻¹ for the 500 kg impactors and 0.002–0.020 cm cell⁻¹ for the 1 g impactors (Table A1). Previous work by Stickle et al. compared 2D axisymmetric simulations to 3D simulations performed in CTH for the same case of an aluminum sphere (radius = 0.635 cm) impacting a bulk strengthless Al 6061 plate at 5 km s⁻¹ at an impact angle of 90° measured from the surface (Stickle et al. 2020). They found that the values for momentum enhancement (β) varied by 19% from 2D to 3D; however, this could be a grid resolution effect, since the 2D cases were performed at cppr = 20 and the 3D case was performed at cppr = 6. They also found that the crater depth and diameters did not significantly differ between 2D and 3D for the aluminum targets. We take this as evidence that 2D axisymmetric cases are comparable to the 3D results produced by CTH.

Target material modeling. This work investigated the effects of target strength on the deflection efficiency of kinetic impacts by defining a weak, moderate, and strong granite target by varying the cohesion strength (Y_0) from 1 to 90 MPa and keeping the tensile strength constant at a relatively high value (–100 MPa). This, however, is not realistic for geologic material, where the tensile strength scales with the cohesion. In order to investigate the effects of tensile strength (σ), we reran case 2 (1 g Cu sphere impacting a strong granite target at 5 km s⁻¹), which originally consisted of $Y_0 = 90$ MPa, $\sigma = -100$ MPa, into three sets of granite targets where both the cohesion and tensile strength were varied. The strong target consisted of $Y_0 = 90$ MPa, $\sigma = -90$ MPa; the moderate consisted of $Y_0 = 45$ MPa, $\sigma = -45$ MPa; and the weak target had $Y_0 = 1$ MPa, $\sigma = -1$ MPa. Figure A1 shows that for a strong target, changing σ from –100 to –90 had little effect on the crater volume (Figure A1(a)) and

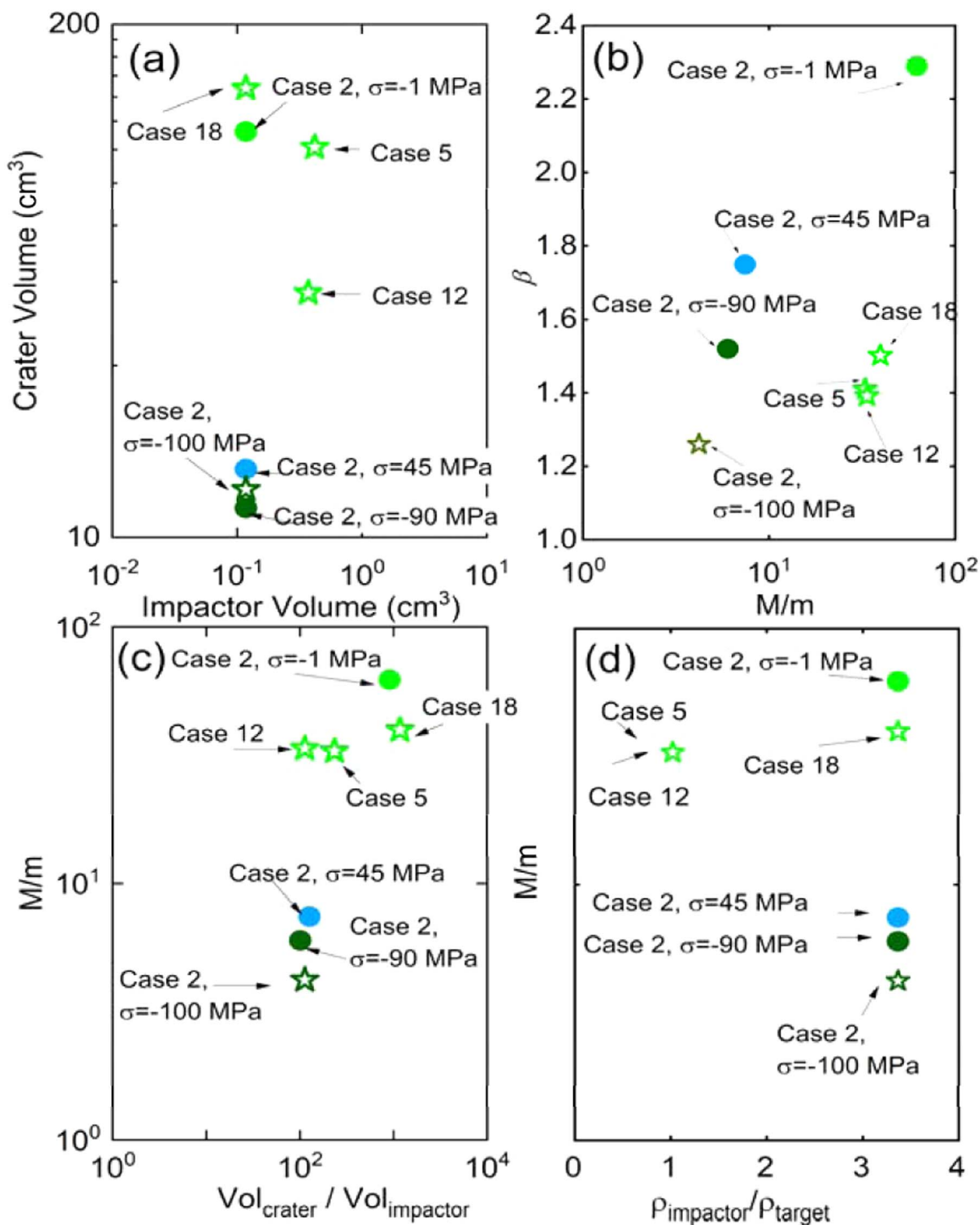


Figure A1. (a) Crater volume as a function of impactor volume. (b) β as a function of normalized ejecta mass. (c) Normalized ejecta mass vs. normalized crater volume. (d) Normalized ejecta mass vs. normalized impactor density for all 1 g impactors with 500 km s⁻¹ impact velocities, where the tensile strength was kept constant at -100 MPa, compared to case 2 (Cu sphere) rerun into strong, medium, and weak targets, where the tensile strength was varied from 1 to 90 MPa.

ejecta mass (Figures A1(c) and (d)); however, it does affect β by 19% (Figure A1(b)). We see that the effects of tensile strength are most apparent for the weak target, where there is evidence for much larger β and ejecta mass compared to cases 5, 12, and 18 that were run with a weak target defined by $Y_0 = 1$ MPa, $\sigma = -100$ MPa. In total, the effects of varying the tensile strength are most pronounced for weaker targets. The lack of a relationship between target strength and the various deflection factors measured in this study (crater size, β , ejecta momentum) was

likely due to the lack of varying tensile strength when modeling targets of varying morphology.

A.3. DOE Results

This section provides the full details of the analysis of the significance testing used to interpret the hydrocode results. Table A2 lists the results used from each CTH simulation to fit and determine a response surface to evaluate the importance of

Table A2
Summary of CTH Results for 18 Impact Cases Considered Here

Case	β	Crater Depth (cm)	Crater Width (cm)	Max Ejecta Mass (g)	Total Ejecta Momentum (g cm s ⁻¹)
1	1.43	186.00	402.00	5.07E+06	1.73E+11
2	1.26	2.19	3.00	4.41	1.98E+04
3	1.01	19.00	93.00	3.25E+04	8.00E+08
4	1.01	84.85	201.00	5.79E+04	2.08E+07
5	1.41	3.19	8.02	3.70E+01	3.47E+05
6	1.01	Two mini craters, each 13.00	Two mini craters, each 40.00	7.20E+03	1.13E+04
7	1.32	121.00	356.00	2.28E+06	1.25E+11
8	1.30	80.00	396.00	2.93E+06	7.31E+10
9	1.00	0.06	0.96	0.20	1.33E+01
10	1.01	0.74	2.26	1.29	2.36E+02
11	1.57	276.00	360.00	7.51E+06	1.41E+11
12	1.39	2.12	6.64	33.55	7.46E+04
13	1.02	0.04	1.30	0.55	7.08E+00
14	1.02	0.80	2.42	2.09	4.13E+02
15	1.01	46.00	162.00	7.23E+04	1.05E+08
16	1.04	103.00	141.00	9.52E+05	8.34E+08
17	1.02	0.37	2.18	0.93	9.23E+02
18	1.50	4.30	7.54	41.54	1.18E+05

Note. Crater size, ejecta properties, and momentum enhancement (β) were recorded for each CTH simulation. The case numbers correspond to the cases in Table 1.

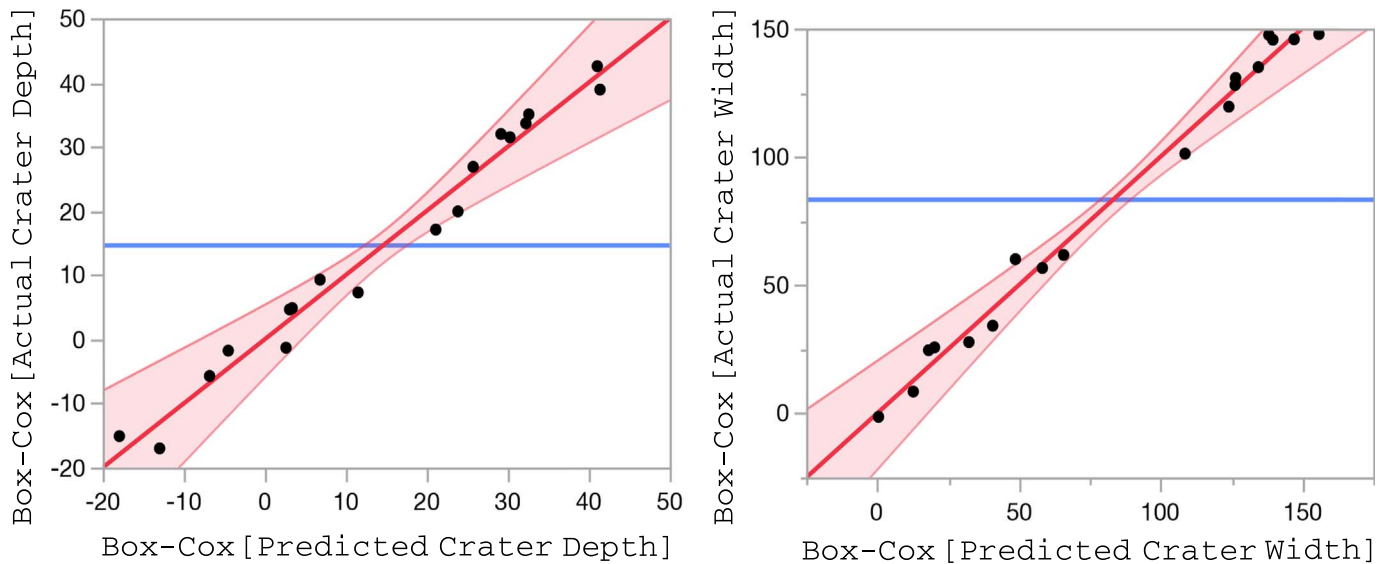


Figure A2. Comparison of actual (black dots) vs. predicted (red line) values from the fit model for crater depth (left) and width (right) using the JMP statistical software. The red shaded area shows the 5%–95% confidence interval on the fit to the model. The fit model includes the following terms: impactor mass, impact velocity, impactor shape, target strength, and impactor composition. The blue line represents the mean value of the y-axis points. Prior to fitting the distribution for crater depth and width, the CTH-derived values were transformed using a Box–Cox transformation with $\lambda = 0.08$ (left; depth) and $\lambda = -0.101$ (right; width) to make the values more normally distributed. The black dots are the transformed crater size values.

each parameter on the final crater size, ejecta properties, and final momentum enhancement. Since normality is an important assumption in order to derive p -values, we impose a Box–Cox transformation on the initial input data. The results of the actual versus predicted values from the fit model for the Box–Cox

transformed data are individually plotted in Figures A2–A4. They show the 5%–95% confidence interval on the fit to the model, where the fit model includes impactor mass, impact velocity, impactor shape, target strength, and impactor composition. The blue line represents the mean value of the y-axis points.

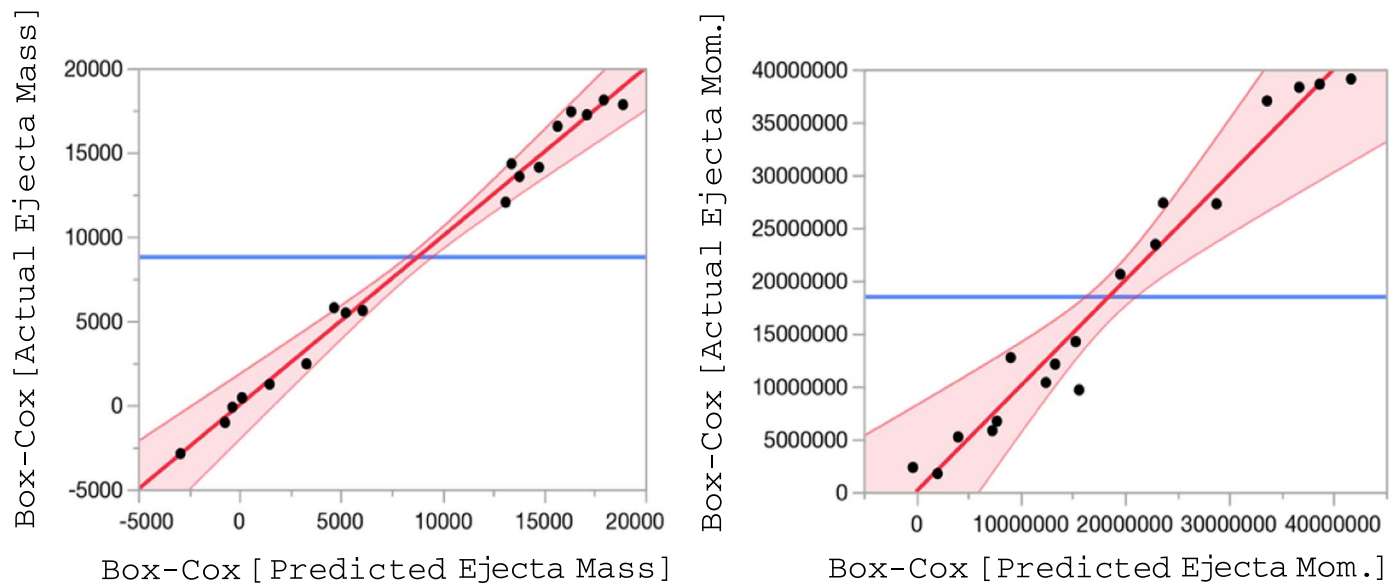


Figure A3. Comparison of actual (black dots) vs. predicted (red line) values from the fit model for the ejecta mass (left) and momentum (right) constructed using the JMP statistical software. The red shaded area shows the 5%–95% confidence interval on the fit to the model. The fit model includes the following terms: impactor mass, impact velocity, impactor shape, target strength, and impactor composition. The black dots are the transformed ejecta mass values. The blue line represents the mean value of the y-axis points. Prior to fitting the distribution for crater depth and width, the values were transformed using a Box–Cox transformation with $\lambda = -0.055$ for the ejecta mass and $\lambda = 0.041$ for the ejecta momentum to make the values more normally distributed.

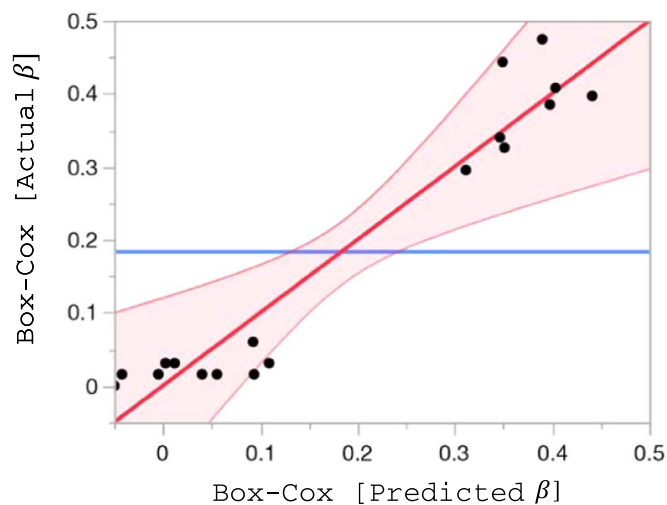




Figure A4. Comparison of actual (black dots) vs. predicted (red line) values from the fit model for momentum enhancement, β , constructed using the JMP statistical software. The red shaded area shows the 5%–95% confidence interval on the fit to the model. The fit model includes the following terms: impactor mass, impact velocity, impactor shape, target strength, and impactor composition. The black dots are the transformed β values. The blue line represents the mean value of the y-axis points. Prior to fitting the distribution for crater depth and width, the values for β were transformed using a Box–Cox transformation with $\lambda = -2$ to make the values more normally distributed.

ORCID iDs

Mallory E. DeCoster  <https://orcid.org/0000-0002-1139-9235>
 Angela M. Stickle  <https://orcid.org/0000-0002-7602-9120>

References

A'Hearn, M. F., Belton, M. J. S., Delamere, W. A., et al. 2005, *Sci*, **310**, 258
 Alvarez, L. W., Alvarez, W., Asaro, F., & Michel, H. V. 1980, *Sci*, **208**, 1095
 Backman, M. E., & Goldsmith, W. 1978, *IJES*, **16**, 1

Bardeen, C. G., Garcia, R. R., Toon, O. B., & Conley, A. J. 2017, *PNAS*, **114**, E7415
 Barnouin, O. S., Daly, M. G., Highsmith, D. E., et al. 2019, *NatGe*, **12**, 247
 Benz, W., Cameron, A. G. W., & Melosh, H. J. 1989, *Icar*, **81**, 113
 Box, G. E. P., & Cox, D. R. 1964, *Journal of the Royal Statistical Society. Series B (Methodological)*, **26**, 211
 Bruck Syal, M., Michael Owen, J., & Miller, P. L. 2016, *Icar*, **269**, 50
 Brundage, A. 2013, *Procedia Engineering*, **58**, 461
 Cheng, A. F., Michel, P., Jutzi, M., et al. 2016, *P&SS*, **121**, 27
 Cheng, A. F., Rivkin, A. S., Michel, P., et al. 2018, *P&SS*, **157**, 104
 Colaprete, A., Schultz, P., Heldmann, J., et al. 2010, *Sci*, **330**, 463
 Collins, G. S., Melosh, H. J., & Ivanov, B. A. 2004, *M&PS*, **39**, 217
 Crawford, D. 1999, Adaptive Mesh Refinement in CTH SAND99-1118C, Sandia National Laboratories, <https://www.osti.gov/biblio/7235>
 Crawford, D. A., Quintana, S. N., & Schultz, P. H. 2013, A Model of Localized Shear Heating with Implications for the Morphology and Paleomagnetism of Complex Craters SAND2013-6319C465175, Sandia National Laboratories, <https://www.osti.gov/servlets/purl/1106416>
 Dearborn, D. P. S., & Miller, P. L. 2015, in Handbook of Cosmic Hazards and Planetary Defense, ed. J. N. Pelton & F. Allahdadi (Cham: Springer), 733
 Elbeshhausen, D., Wünnemann, K., & Collins, G. S. 2009, *Icar*, **204**, 716
 French, B. M. 1998, Traces of Catastrophe: A Handbook of Shock-Metamorphic Effects in Terrestrial Meteorite Impact Structures (Houston, TX: Lunar and Planetary Institute), 954
 Goos, P., & Jones, B. 2011, Optimal Design of Experiments: A Case Study Approach (West Sussex, UK: Wiley)
 Grady, D. E., & Winfree, N. A. 2001, *IJIE*, **26**, 249
 Harvey, E. N. 1948, PAPHS, **92**, 294, <https://www.jstor.org/stable/3143359>
 Heberling, T., Gislser, G., Plesko, C., & Weaver, R. 2017, *Procedia Engineering*, **204**, 124
 Hertel, E. S., Bell, R. L., Elrick, M. G., et al. 1995, in Shock Waves @ Marseille I, ed. R. Brun & L. Z. Dumitrescu (Berlin: Springer), 377
 Holsapple, K. A. 1993, *AREPS*, **21**, 333
 Holsapple, K. A., & Housen, K. R. 2012, *Icar*, **221**, 875
 Ikeda, M., Tanaka, M., Yokoo, D., Koura, T., & Akahoshi, Y. 2017, *Procedia Engineering*, **204**, 138
 Jones, B., & Nachtsheim, C. J. 2011, *JQT*, **43**, 1
 Kipp, M., & Melosh, H. 1986, *LPSC*, **17**, 420
 McGlaun, J. M., Thompson, S. L., & Elrick, M. G. 1990, *IJIE*, **10**, 351
 National Research Council 2010, Defending Planet Earth: Near-Earth-Object Surveys and Hazard Mitigation Strategies (Washington, DC: The National Academies Press), 152
 Pierazzo, E., Vickery, A. M., & Melosh, H. J. 1997, *Icar*, **127**, 408

- Pierazzo, E., Artemieva, N., Asphaug, E., et al. 2008, *M&PS*, **43**, 1917
- Popova, O. P., Jenniskens, P., Emel'yanenko, V., et al. 2013, *Sci*, **342**, 1069
- Raducan, S. D., Davison, T. M., Luther, R., & Collins, G. S. 2019, *Icar*, **329**, 282
- Rainey, E. S. G., Stickle, A. M., Cheng, A. F., et al. 2020, *IJIE*, **142**, 103528
- Rivkin, A. S., Chabot, N. L., Stickle, A. M., et al. 2021, *PSJ*, **2**, 173
- Robertson, D. K., & Mathias, D. L. 2019, *Icar*, **327**, 36
- Sakatani, N., Tanaka, S., Fukuhara, T., et al. 2021, *NatAs*, **5**, 766
- Santner, T. J., Williams, B. J., & Notz, W. I. 2014, *The Design and Analysis of Computer Experiments* (New York: Springer)
- Scheeres, D. J., McMahon, J.W., French, A.S., et al. 2019, *NatAs*, **3**, 352
- Schulte, P., Alegret, L., Arenillas, I., et al. 2010, *Sci*, **327**, 1214
- Schultz, P. H., Hermalyn, B., Colaprete, A., et al. 2010, *Sci*, **330**, 468
- Schultz, P. H., Hermalyn, B., & Veverka, J. 2013, *Icar*, **222**, 502
- Schultz, P. H., & Crawford, D. A. 2016, *Natur*, **535**, 391
- Senft, L. E., & Stewart, S. T. 2009, *E&PSL*, **287**, 471
- Stefanopoulos, P. K., Hadjigeorgiou, G. F., Filippakis, K., & Gyftokostas, D. 2014, *Journal of Acute Disease*, **3**, 178
- Steinberg, D. J., & Lund, C. M. 1989, *JAP*, **65**, 1528
- Stickle, A. M., Atchison, J. A., Barnouin, O. S., et al. 2015, *Procedia Engineering*, **103**, 577
- Stickle, A. M., Bruck Syal, M., Cheng, A. F., et al. 2020, *Icar*, **338**, 113446
- Taylor, P. A. 1992, CTH Reference Manual: The Steinberg- Guinan-Lund Viscoplastic Model Rep. No. SAND92-0716, Sandia National Laboratories
- Tedeschi, W. J., Remo, J. L., Schulze, J. F., & Young, R. P. 1995, *IJIE*, **17**, 837
- Thompson, S. L., & Lauson, H. S. 1974, Improvements in the CHART D radiation-hydrodynamic code III: revised analytic equations of state Rep. No. SC-RR-71-0714, Sandia National Laboratories, <https://www.osti.gov/biblio/4208328-improvements-chart-radiation-hydrodynamic-code-iii-revised-analytic-equations-state>
- Tillotson, J. H. 1962, *Metallic Equations of State For Hypervelocity Impact*. General Atomic Report, Air Force Special Weapons Center, **GA-3216**
- Trucano, T. G., & McGlaun, J. M. 1990, *IJIE*, **10**, 601
- United Launch Alliance, LLC 2021, Atlas V Specifications, <https://www.ulalaunch.com/rockets/atlas-v>
- Walker, J. D., Chocron, S., Durda, D. D., et al. 2013, *Procedia Engineering*, **58**, 240
- Walker, J. D., Chocron, S., & Grosch, D. J. 2020, *IJIE*, **135**, 103388